
TEMPERATURE FIELD INVERSION OF HEAT-SOURCE SYSTEMS VIA PHYSICS-INFORMED NEURAL NETWORKS

A PREPRINT

Xu Liu

Defense Innovation Institute
Chinese Academy of Military Science
China
liuxu18054448691@126.com

Wei Peng

Defense Innovation Institute
Chinese Academy of Military Science
China
weipeng0098@126.com

Zhiqiang Gong

Defense Innovation Institute
Chinese Academy of Military Science
China
gongzhiqiang13@nudt.edu.cn

Weien Zhou

Defense Innovation Institute
Chinese Academy of Military Science
China
weienzhou@outlook.com

Wen Yao *

Defense Innovation Institute
Chinese Academy of Military Science
China
Wendy0782@126.com

January 19, 2022

ABSTRACT

Temperature field inversion of heat-source systems (TFI-HSS) with limited observations is essential to monitor the system health. Although some methods such as interpolation have been proposed to solve TFI-HSS, those existing methods ignore correlations between data constraints and physics constraints, causing the low precision. In this work, we develop a physics-informed neural network-based temperature field inversion (PINN-TFI) method to solve the TFI-HSS task and a coefficient matrix condition number based position selection of observations (CMCN-PSO) method to select optima positions of noise observations. For the TFI-HSS task, the PINN-TFI method encodes constrain terms into the loss function, thus the task is transformed into an optimization problem of minimizing the loss function. In addition, we have found that noise observations significantly affect reconstruction performances of the PINN-TFI method. To alleviate the effect of noise observations, the CMCN-PSO method is proposed to find optima positions, where the condition number of observations is used to evaluate positions. The results demonstrate that the PINN-TFI method can significantly improve prediction precisions and the CMCN-PSO method can find good positions to acquire a more robust temperature field.

Keywords Temperature field inversion of heat-source systems · Physics-informed neural network · Position selection · Condition number · Upper bound of error

*Corresponding author

1 Introduction

Heat management [Grujicic et al., 2005, Laloya et al., 2015] is essential for heat-source systems (HSS), where heat is generated internally, especially over systems that involve components with smaller size and higher power density. Statistically, when the allowable temperature is exceeded [Emam et al., 2019], the failure rate of such electronic devices doubles for the temperature rise of $10 \sim 20^\circ\text{C}$, and its failure rate decreases by about 4 % for the temperature reduction of 1°C . Temperature monitoring is of importance to ensure the normal work of components in heat management systems. Temperature field inversion (TFI) through limited temperature transducers (observations) is an important method to monitor component temperatures [Evans et al., 2002, Kong et al., 2020]. Generally, TFI requires a large number of temperature transducers (observations), which causing expensive costs and affecting the availability of systems. Moreover, too many transducers are not accessible in most real-life applications, which increases the difficulty to reconstruct the whole temperature field. Therefore, temperature field inversion of heat-source systems (TFI-HSS) in a small data setting is an urgent and challenging problem to be solved in practical engineering systems.

The mechanism of the TFI calculation and the temperature adjustment is complicated, thus it is difficult to reconstruct the temperature field through reasonable formula transformations. Interpolation is an easy-implement but low-precision procedure [Steffensen, 2006]. A range of interpolation methods essentially use discrete points to fit the function, such as Gaussian process regression (kriging) [Stein, 2012], random forest regression [Segal, 2004], nearest neighbor [Jiang and Wang, 2015]. In addition to this, reconstructing intensities of heat sources is also a feasible method to reconstruct the temperature field. A boundary element method has been proposed [Le Niliot and Lefèvre, 2001, Le Niliot et al., 2000] to identify intensities of point-heat sources, which is a time regularization based procedure. Two sources that have different shapes and close distances may cause inaccurate estimations. To this end, a numerical algorithm coupled with the concept of future time is proposed [Yang, 1999]. Subsequently, Shuai et al. [2011] propose an adaptive iterative algorithm. They regard intensities as variables and then use a multivariate iterative approach to minimize the discrepancy between prediction and measurements. This iterative method has a large search space and is low efficient, which is appropriate to solve reconstruction problems with a small number of iterations. In the small data setting, these existing TFI methods ignore correlations between data constraints and physics constraints (governing equations), resulting in low precisions and even unavailability.

Recently, physics-informed neural networks (PINNs) have been successfully used to solve partial differential equations (PDEs) or PDE-based problems [Raissi et al., 2019, Shen et al., 2021, Zobeiry and Humfeld, 2021] by adding data constraints and physics constraints in the loss function to constrain the space of admissible solutions. Then, the problem of solving PDEs is transformed into an optimization problem of minimizing the loss function. Furthermore, benefited from physics constraints, the PINN can reduce the requirement of label data and be easily applied to the small data regime. In addition, compared to traditional numerical approaches such as finite difference method [Narasimhan and Witherspoon, 1976], mesh-free PINNs can easily solve irregular-domain problems [Gao et al., 2020] and avoid the curse of dimensionality [Grohs et al., 2018]. Moreover, PINNs have offered a powerful new paradigm for dealing with diverse inverse problems, including systems biology [Yazdani et al., 2020], hidden fluid mechanics [Raissi et al., 2020, Tartakovsky et al., 2020], biomedicine [Sahli Costabal et al., 2020, Kissas et al., 2020] and the parameter identification of wave, stochastic and fractional PDEs [Song and Alkhalifah, 2020, Tartakovsky et al., 2020, Pang et al., 2019]. By introducing a data-constrained term with the mean-squared error, Pang et al. [Pang et al., 2019] use PINNs to identify the diffusion coefficients in fractional advection-diffusion equations from synthetic data. Subsequently, parameterizing the data-constrained term as polynomial functions by prior knowledge, Chen et al. [Chen et al., 2021a] extend PINNs to solve the inverse problem that the initial probability density function of Fokker-Plank equations is agnostic. Similarly, considering the unknowable initial and boundary condition, PINNs are employed to reconstruct the flow field based on scattered observation about the velocity [Raissi et al., 2020, Tartakovsky et al., 2020]. For higher-dimensional problems, PINNs are employed by Kissas et al. [Kissas et al., 2020] to recover the entire three-dimensional velocity flow field given four-dimensional flow magnetic resonance imaging data, which shows that PINNs have a great feature for high-dimensional and real-life problems. TFI-HSS is essentially an inverse problem, where intensities of heat sources are unknown. Thus, PINNs are promising for solving TFI-HSS.

However, there still exist two major difficulties in applying PINNs to solve TFI-HSS.

- Using PINNs to reconstruct efficiently the temperature field is an urgent problem, given a limited number of observations and the governing equation.
- Observations are inevitably perturbed in real-life engineering systems. Given noise observations, positions of observations significantly affect the reconstructed performance. At present, there is no appropriate strategy to choose reasonable positions to alleviate the effect of noises.

To solve the first issue, we employ the physics characteristic and develop a novel physics-informed neural network-based temperature field inversion (PINN-TFI) method to solve TFI-HSS. The PINN-TFI method encodes physics and data

constraint terms into the loss function, thus the problem of TFI-HSS is transformed into an optimization problem of minimizing the physics-informed loss function. In addition, large computational costs are one of main limitations of the PINN for TFI-HSS. In prior works, transfer learning has been widely used to improve the convergence of training for diverse deep learning problems [Yang et al., 2013]. Inspired by this idea, we first utilize transfer learning to obtain a retrained PINN and then use the retrained PINN with observations for TFI. To solve the latter one, we develop a coefficient matrix condition number based position selection of observations (CMCN-PSO) method, where the condition number of noise observations is used to evaluate positions. In summary, the following contributions are made in this paper.

- We refine the Temperature Field Inversion of Heat-Source Systems (TFI-HSS) task from engineering applications by giving the formula expression.
- We propose a physics-informed neural network-based temperature field inversion (PINN-TFI) method to reconstruct the temperature field, where transfer learning strategy is used to accelerate the training process.
- We develop a coefficient matrix condition number based position selection of observations (CMCN-PSO) method to alleviate the effect of noise observations for the PINN-TFI method.

The experiments considering three types of boundary conditions have been conducted. Experiment results show that the PINN-TFI method has superior performance for the TFI-HSS task. Moreover, the CMCN-PSO method can find good positions of observations. Given noise observations, the PINN-TFI method uses these observations to reconstruct a more robust temperature field.

2 Temperature Field Inversion of Heat-Source Systems (TFI-HSS)

Heat-source systems (HSS) will be discussed in this chapter, where observations and the principle of heat transfer equations are taken into account. In this work, HSS is modeled as a two-dimensional plane. There are several electronic components on this plane and these components generate heat when working. Each component is simplified as a heat source. The purpose of the TFI-HSS task is to reconstruct the temperature field given some observations, which is very important to ensure working temperatures of components and monitor the HSS health.

Generally, given a HSS with m observations, the TFI-HSS task can be written as

$$\arg \min_{\theta} \left(\sum_{i=1}^m |T_{\theta}(x_{obs}^i, y_{obs}^i | \phi) - T_{obs}^i(x_{obs}^i, y_{obs}^i)| \right), \quad (1)$$

where $T_{\theta}(\cdot)$ is the model with the parameter θ to reconstruct the temperature field, unknown ϕ is the intensity distribution, and T_{obs}^i represents the temperature of observations. In addition, the stead-state temperature field T has to satisfy

$$\begin{aligned} \frac{\partial}{\partial x} (k \frac{\partial T}{\partial x}) + \frac{\partial}{\partial y} (k \frac{\partial T}{\partial y}) + \phi(x, y) &= 0, \\ \text{Boundary : } T = T_0 \quad \text{or} \quad k \frac{\partial T}{\partial \mathbf{n}} &= 0 \\ \quad \quad \quad \text{or} \quad k \frac{\partial T}{\partial \mathbf{n}} &= h(T - T_0), \end{aligned} \quad (2)$$

where k is the thermal conductivity and is set to be 1 in this work, ϕ is the intensity distribution function, and T_0 is the temperature value of the isothermal boundary or the convective boundary conditions. Eq.(2) represents three boundary conditions including Dirichlet (isothermal), Neumann (adiabatic), and Robin (convective) boundary conditions, where h denotes the convective heat transfer coefficient.

The area of a single piece of heat source is set as a rectangle in this work, modeled as

$$\phi(x, y) = \begin{cases} \phi_i, & (x, y) \in \Gamma_i, i = 1, 2, \dots, n \\ 0, & (x, y) \notin \Gamma_i \end{cases}, \quad (3)$$

where ϕ_i represents the (constant) intensity of i th heat source, Γ_i represents the area of i th heat source, and n is the number of heat sources. In summary, the TFI-HSS task can be expressed as a constrained optimization problem, which is formulated as

$$\begin{aligned} \min_{\theta} & \left(\sum_{i=1}^m |T_{\theta}(x_{obs}^i, y_{obs}^i | \phi) - T_{obs}^i(x_{obs}^i, y_{obs}^i)| \right), \\ \text{s.t.} & \quad \frac{\partial}{\partial x} (k \frac{\partial T}{\partial x}) + \frac{\partial}{\partial y} (k \frac{\partial T}{\partial y}) + \phi(x, y) = 0, \\ & \quad T = T_0 \quad \text{or} \quad k \frac{\partial T}{\partial \mathbf{n}} = 0 \quad \text{or} \quad k \frac{\partial T}{\partial \mathbf{n}} = h(T - T_0). \end{aligned} \quad (4)$$

For further research on the TFI-HSS task, the volume-to-point (VP) and the volume-to-boundary (VB) problems are commonly used in heat conduction problems [Aslan et al., 2018, Chen et al., 2016, 2021b]. From the perspective of mathematical models, the difference between VB and VP problems is the boundary condition. For the VP heat conduction problem, it considers a finite heat-generating volume cooled by a small patch of the common heat sink with the temperature of T_0 located on the middle of the bottom boundary, shown in Fig. 1(a). For the VB problem, the condition of each boundary can be isothermal, adiabatic, or convective, shown in Fig. 1(b).

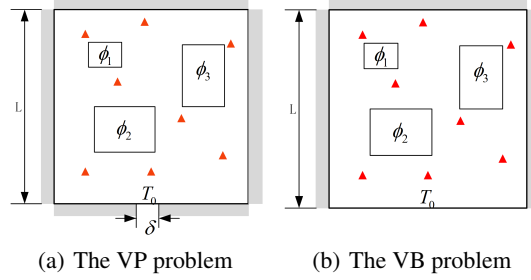


Figure 1: The illustration of the VP and the VB problem in a square domain.

3 Methodology

3.1 Overview

For the TFI-HSS task, given the unknown intensity distribution, temperature field $T(x, y)$ can not be solved numerically by discretizing Eq.(2) using the finite difference method [Narasimhan and Witherspoon, 1976] or the finite volume method [Eymard et al., 2000]. Interpolations can reconstruct the temperature field. However, reconstruction errors are high and costs of much observation acquisition are prohibitive. Moreover, the vast majority of state-of-the-art machine learning techniques (e.g., deep/convolutional/recurrent neural networks) may become intractable when it comes to the small data regime. To this end, a novel Physics-Informed Neural Network-based Temperature Field Inversion (PINN-TFI) method is proposed to reconstruct the temperature field in the small data setting. The PINN-TFI method is expected to provide a rapid and accurate prediction of the temperature field. In addition, we have found that noise observations significantly affect reconstructed performance of the PINN-TFI method but reasonably position selection of observations can alleviate the effect of noise observations. In this work, a coefficient matrix condition number based position selection of observations (CMCN-PSO) method is proposed to find optimal positions of noise observations. Then, the optimal observations are used by the PINN-TFI method to reconstruct a more robust temperature field. A schematic diagram of the PINN-TFI method and the CMCN-PSO method is shown in Fig. 2. Details of the PINN-TFI method and the CMCN-PSO method will be presented in the following subsections.

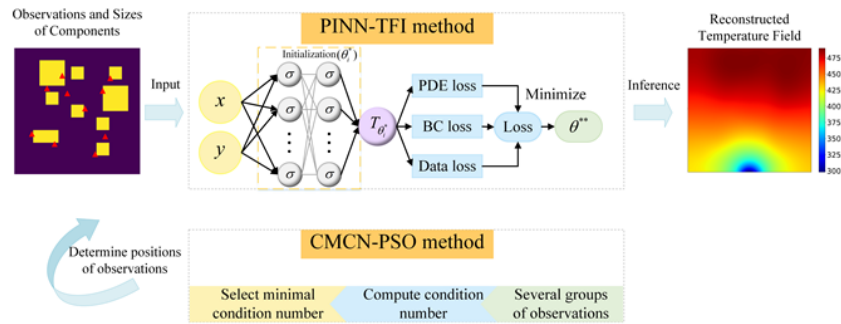


Figure 2: Conceptual flow of the PINN-TFI method and the CMCN-PSO method.

3.2 Physics-informed neural network-based temperature field inversion (PINN-TFI) method

TFI-HSS can be considered as an inverse problem, where the temperature field can be learned from observations. To solve the inverse problem, we propose a Physics-Informed Neural Network based temperature field inversion

(PINN-TFI) method, where the transfer learning strategy is used to accelerate the training process. Concretely, the weights and biases for predicting a new temperature field are initialized with those for the temperature field under rated intensity values. Then, the weights and biases are trained to learn from observations. The PINN-TFI method is mainly divided into two parts, namely the model initialization and the model for temperature field inversion, and its detailed description is in algorithm 1. The key of the PINN-TFI method is that the constrained optimization problem of TFI-HSS is transformed into an unconstrained optimization problem of minimizing the loss function by adding data and physics constrain terms to the loss function.

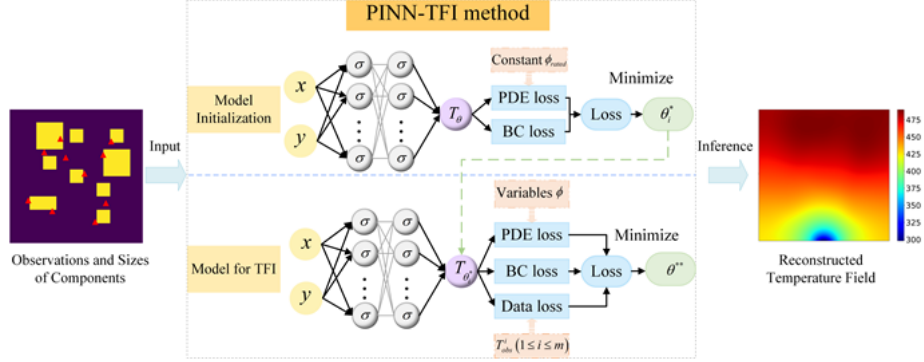


Figure 3: Conceptual flow of the PINN-TFI method with observations.

Let $T_\theta(\cdot)$ be a NN of depth D , where θ is the vector of weights and bias. The NN has an input layer, $D - 2$ hidden layers and an output layer, which is a mapping from \mathbb{R}^d into \mathbb{R}^N . In this work, a Multi-Layer Perception (MLP) is employed with the activation function $\sigma(\cdot)$, i.e.,

$$T_\theta := L_D \circ \sigma \circ L_{D-1} \circ \sigma \circ \dots \circ \sigma \circ L_1, \quad (5)$$

where

$$\begin{aligned} L_1(x) &:= W_1 x + b_1, & W_1 &\in \mathbb{R}^{d_1 \times d}, b_1 \in \mathbb{R}^{d_1}, \\ L_k(x) &:= W_k x + b_k, & W_{ik} &\in \mathbb{R}^{d_k \times d_{k-1}}, b_k \in \mathbb{R}^{d_k}, \\ L_D(x) &:= W_D x + b_D, & W_D &\in \mathbb{R}^{N \times d_{D-1}}, b_D \in \mathbb{R}^N. \end{aligned} \quad (6)$$

The model initialization: The rated intensity distribution ϕ_{rated} of heat sources is available. PINNs are employed to solve Eq.(2) without observations and obtain initialization parameter θ_i^* . The left-hand-side of Eq.(2) is first defined as

$$f = \frac{\partial}{\partial x} \left(k \frac{\partial T}{\partial x} \right) + \frac{\partial}{\partial y} \left(k \frac{\partial T}{\partial y} \right) + \phi(x, y). \quad (7)$$

Then, the training sets \mathcal{P}_{pde}^i and \mathcal{P}_{bc}^i for PDE and boundary conditions (e.g., randomly sampling points in the domain and boundary) are specified. To measure the difference between the NN and physics constraints, the loss function including partial differentiable equation loss (PDE loss), boundary condition loss (BC loss) is defined by

$$\mathcal{L}_{PINN}^i(\theta) = w_{pde}^i \mathcal{L}_{pde}^i + w_{bc}^i \mathcal{L}_{bc}^i, \quad (8)$$

where

$$\begin{aligned} \mathcal{L}_{pde}^i &= \frac{1}{|\mathcal{P}_{pde}^i|} \sum_{(\mathbf{x}, \mathbf{y}) \in \mathcal{P}_{pde}^i} \|f(T_\theta, x, y, \phi_{rated})\|_2^2, \\ \mathcal{L}_{bc} &= \frac{1}{|\mathcal{P}_{bc}^i|} \sum_{(\mathbf{x}, \mathbf{y}) \in \mathcal{P}_{bc}^i} \|T_\theta - T_0\|_2^2 \quad or \\ \mathcal{L}_{bc} &= \frac{1}{|\mathcal{P}_{bc}^i|} \sum_{(\mathbf{x}, \mathbf{y}) \in \mathcal{P}_{bc}^i} \left\| k \frac{\partial T_\theta}{\partial \mathbf{n}} \right\|_2^2, \end{aligned} \quad (9)$$

and w_{pde}^i as well as w_{bc}^i are weight hyper-parameters, which need to be predefined. \mathcal{P}_{pde}^i and \mathcal{P}_{bc}^i denote the sets of residual points from PDE and boundary conditions, respectively.

Finally, the NN is trained by minimizing the loss function $\mathcal{L}_{PINN}(\theta)^i$ until finding the best parameters θ_i^* .

The model for temperature field inversion: First, transfer learning strategy is used to initialize the NN model with parameter θ_i^* for accelerating the training process. When components are working normally, then real intensity

Algorithm 1: The Physics-Informed Neural Network-based Temperature Field Inversion method (PINN-TFI method)

Input:

ϕ_{rated} , the intensity distribution function under the rated powers,
 $\mathcal{P}_{data} = \{T(x_{obs}^i, y_{obs}^i), i = 1, \dots, n\}$, the observation set.

Output:

$\hat{T}(x, y, \theta^{**})$ as the surrogate of the temperature field

- 1 Construct a NN with the parameter θ , $T_\theta(\cdot)$.
 - 2 // **The model initialization**
 - 3 Specify two training sets \mathcal{P}_{pde}^i and \mathcal{P}_{bc}^i for PDE and boundary conditions.
 - 4 Calculate PDE loss L_{pde}^i and BC loss L_{bc}^i by Eq.(9).
 - 5 Obtain total loss $L_{PINN}^i(\theta)$ by Eq.(8).
 - 6 Train the NN by minimizing the loss function $\mathcal{L}_{PINN}(\theta)$ until finding the best parameters θ_i^* .
 - 7 // **The model for temperature field inversion**
 - 8 The NN is initialized with the parameter θ_i^* .
 - 9 Specify two training sets \mathcal{P}_{pde} and \mathcal{P}_{bc} for PDE and boundary conditions and confirm \mathcal{P}_{data} .
 - 10 Set ϕ to be a variable initialized with the value ϕ_{rated} and put it in the optimizer.
 - 11 Calculate the L_{pde} , L_{bc} and L_{data} by Eq.(11).
 - 12 Obtain the $L_{PINN}(\theta_i^*)$ by Eq.(10).
 - 13 Train the NN by minimizing the loss $L_{PINN}(\theta_i^*)$ until finding the best parameters θ^{**} .
-

distribution ϕ is unknown, which is set to be a variable initialized the value ϕ_{rated} and is put in the optimizer as trainable parameters. In addition to training sets \mathcal{P}_f and \mathcal{P}_{bc} for PDE and boundary conditions, the observation set \mathcal{P}_{data} is confirmed. By adding a data constrained term, the loss function is formulated as

$$\mathcal{L}_{PINN}(\theta_i^*) = w_{pde}\mathcal{L}_{pde} + w_{bc}\mathcal{L}_{bc} + w_{data}\mathcal{L}_{data}, \quad (10)$$

where

$$\begin{aligned} \mathcal{L}_{pde} &= \frac{1}{|\mathcal{P}_{pde}|} \sum_{(\mathbf{x}, \mathbf{y}) \in \mathcal{P}_{pde}} \|f(T_{\theta_i^*}, x, y, \phi)\|_2^2, \\ \mathcal{L}_{data} &= \frac{1}{|\mathcal{P}_{data}|} \sum_{(\mathbf{x}, \mathbf{y}) \in \mathcal{P}_{data}} \|T_{\theta_i^*} - T_{obs}\|_2^2, \\ \mathcal{L}_{bc} &= \frac{1}{|\mathcal{P}_{bc}|} \sum_{(\mathbf{x}, \mathbf{y}) \in \mathcal{P}_{bc}} \|T_{\theta_i^*} - T_0\|_2^2 \quad or \\ \mathcal{L}_{bc} &= \frac{1}{|\mathcal{P}_{bc}|} \sum_{(\mathbf{x}, \mathbf{y}) \in \mathcal{P}_{bc}} \left\| k \frac{\partial T_{\theta_i^*}}{\partial \mathbf{n}} \right\|_2^2, \end{aligned} \quad (11)$$

and w_{pde} , w_{bc} as well as w_{data} are predefined weight hyper-parameters. Thus, the constrained optimization problem in Eq.(2) is transformed into an unconstrained optimization problem of minimizing the loss $\mathcal{L}_{PINN}(\theta_i^*)$ in Eq.(10). In the last step, the training procedure is to search for the best parameter θ^{**} by minimizing the loss $\mathcal{L}_{PINN}(\theta_i^*)$, where *automatic differentiation* is used to minimize the highly nonlinear and non-convex loss.

In summary, the PINN-TFI-method can reconstruct the temperature field with limited observations. However, in real-life engineering systems, observations are inevitably perturbed by noises, which significantly affects reconstruction performances of the PINN-TFI-method. We have found that reasonable position selection of observations can alleviate the effect of noise observations.

3.3 The coefficient matrix condition number based position selection of observations method

In this chapter, we propose a coefficient matrix condition number based position selection of observations (CMCN-PSO) method to alleviate the effect of noise observations. First, the finite difference method is utilized to discretize the governing equation, where the unknown intensity is set to be a variable. Then, combing with matrix forms about observations, the constrained optimization problem of TFI-HSS in Eq.(4) is transformed into an unconstrained optimization problem by the penalty method. Furthermore, through analyses of noise observations, the upper bound of the reconstruction error is proved to be related to the coefficient matrix condition number, which is determined by positions of observations. After that, the condition number becomes the principle to evaluate positions of observations from many groups of positions. Many groups of positions are sampled by Latin hypercube, low discrepancy and grid-based sampling methods in this work. Finally, the optimal positions corresponding to the minimum condition number are selected. The CMCN-PSO method is described in Algorithm 2 and the detail steps are as follows.

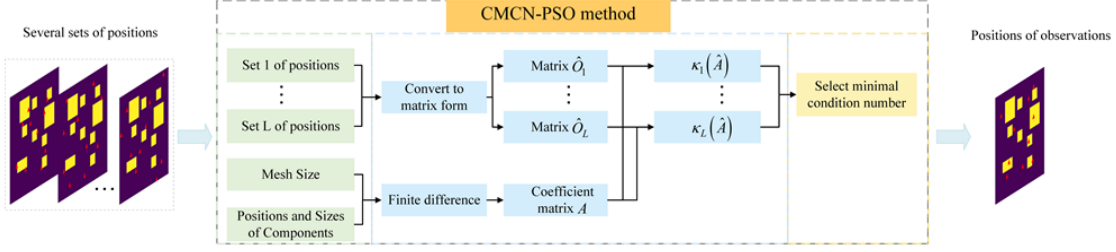


Figure 4: Conceptual flow of the CMCN-PSO method with observations.

Algorithm 2: A coefficient matrix condition number based position selection of observations (CMCN-PSO) method

Input:

$\{(x_1, y_1), \dots, (x_m, y_m)\}, \dots, \{(x_{Lm+1}, y_{Lm+1}), \dots, (x_{(L+1)m}, y_{(L+1)m})\}$, several sets of positions.
 The positions and sizes of n components

The mesh size $K \times K$

Output:

The optimal position of observations $\hat{O}_{optimal}$

- 1 // Determine the coefficient matrix A
 - 2 Mesh the domain as a $K \times K$ grid system and mesh the components in the grid system
 - 3 Number the $K \times K$ grid points from left to right, bottom to top
 - 4 Calculate the coefficient matrix A_1 by finite difference according to the boundary conditions
 - 5 **for** $i=1, 2, \dots, K$ **do**
 - 6 **if** grid points is location in the components' area **then**
 - 7 Set the i th row of the maxtrix A_2 to $-h^2$
 - 8 **else**
 - 9 Set the i th row of the maxtrix A_2 to 0
 - 10 **end**
 - 11 **end**
 - 12 Construct the matrix A by $A = (A_1, A_2)^T$
 - 13 // Determine the matrix \hat{O} according to positions of observations
 - 14 **for** $j=1, 2, \dots, L$ **do**
 - 15 **for** $i=1, 2, \dots, n$ **do**
 - 16 Set the i th column of the maxtrix \hat{O}_j to 1 and other columns to 0
 - 17 **end**
 - 18 **end**
 - 19 // Calculate the condition number
 - 20 Calculate the condition number of \hat{A} by the function (e.g., $np.linalg.cond(\hat{A})$)
 - 21 **for** $j=1, 2, \dots, L$ **do**
 - 22 $\kappa_j(\hat{A}) = cond((\lambda A, \hat{O}_j)^T)$ (λ is set to be 1 in this work)
 - 23 **end**
 - 24 //Select the optimal positions
 - 25 Select the minimal condition number $\kappa_{optimal} = \min(\kappa_1, \dots, \kappa_L)$
 - 26 Find the optimal positions $\hat{O}_{optimal}$ (corresponding to $\kappa_{optimal}$)
-

The two-dimensional domain is first discretized by using a Cartesian shown in Fig. 5. The grid points are divided into boundary points (red) and internal points (black). The temperatures of boundary points are controlled by boundary conditions. The governing equation in Eq.(4) is discretized by the finite difference method, which is written as

$$-4t_{i,j} + t_{i-1,j} + t_{i+1,j} + t_{i,j-1} + t_{i,j+1} = h^2\phi, \quad (12)$$

where $1 \leq i, j \leq K$ and $t_{j,k}$ denotes the temperature value of node (i, j) and h is the step length of two adjacent nodes. Assume that the two-dimensional domain is meshed as a $K \times K$ system and the temperature of the grid points is sorted as $T_{m \times 1} = (t_1, t_2, \dots, t_m)^T$, $m = K \times K$. The governing equation and boundary conditions in Eq.(4) are expressed

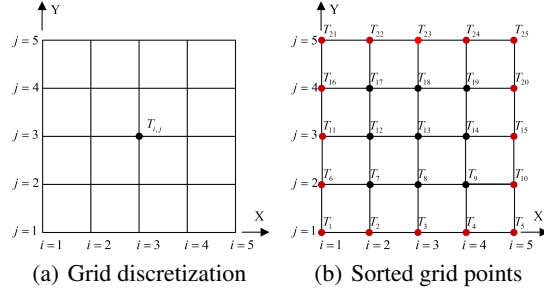


Figure 5: The grid discretization of the two-dimensional domain.

as

$$A_1 \cdot T = h^2 \phi + C_1, \quad (13)$$

where

$$A_1 = \begin{bmatrix} \mathbf{V} + 2\mathbf{I} & -\mathbf{I} & 0 \\ -\mathbf{I} & \mathbf{V} + 2\mathbf{I} & -\mathbf{I} \\ 0 & -\mathbf{I} & \mathbf{V} + 2\mathbf{I} \end{bmatrix}_{m \times m} \quad (14)$$

is the coefficient matrix and $\mathbf{V} = \text{tridiag}_L(-1, 2, -1) \in \mathbb{R}^{L,L}$. C_1 is a vector that contains boundary values. Given the HSS with n heat sources, ϕ_i forms a matrix $Y_{n \times 1} = (\phi_1, \phi_2, \dots, \phi_n)^T$. According to Eq.(3), ϕ can also be expressed as

$$\begin{aligned} \phi &= \begin{pmatrix} b_{1,1} & \dots & b_{1,n} \\ \vdots & \ddots & \vdots \\ b_{s,1} & \dots & b_{m,n} \end{pmatrix}_{m \times n} \begin{pmatrix} \phi_1 \\ \phi_2 \\ \vdots \\ \phi_n \end{pmatrix}_{n \times 1} \\ &= B_{m \times n} Y_{n \times 1}, \end{aligned} \quad (15)$$

where $b_{i,j}$ is equal to 0 or 1. When the grid point of t_i ($1 \leq i \leq m$) is located in the area Γ_j ($1 \leq j \leq n$), $b_{i,j}$ is equal to 1 and otherwise $b_{i,j}$ is set to be 0. Then, Eq.(13) is simplified as

$$A\hat{T} = (A_1, -h^2 B) \begin{pmatrix} T \\ Y \end{pmatrix} = C_1. \quad (16)$$

The constraint of the optimization problem in Eq.(4) can be described by Eq.(16) and the optimization objective can be written as

$$\min \left\| \hat{O}\hat{T} - C_2 \right\|_2^2 = \min \left\| \begin{pmatrix} O & 0 \end{pmatrix} \begin{pmatrix} T \\ Y \end{pmatrix} - C_2 \right\|_2^2, \quad (17)$$

where O is a matrix describing positions of observations, and C_2 is a matrix containing T_{obs}^i ($1 \leq i \leq m$). The matrix O has only 1 in each row and the rest are 0. For example, there are three observations in grid node 1, 2 and 5. $\hat{O}\hat{T} - C_2$ can be expressed as

$$\begin{pmatrix} 1 & 0 & 0 & 0 & 0 & \dots & 0 \\ 0 & 1 & 0 & 0 & 0 & \dots & 0 \\ 0 & 0 & 0 & 0 & 1 & \dots & 0 \end{pmatrix}_{3 \times m} \hat{T}_{m \times 1} - \begin{pmatrix} T_{obs}^1 \\ T_{obs}^2 \\ 0 \\ T_{obs}^3 \\ \vdots \\ 0 \end{pmatrix}_{m \times 1}. \quad (18)$$

Therefore, the optimization problem of the TFI-HSS task is formulated by

$$\begin{aligned} \min & \left\| \hat{O}\hat{T} - C_2 \right\|_2^2, \\ \text{s.t.} & A\hat{T} = C_1, \end{aligned} \quad (19)$$

which can be transformed into an unconstrained problem by the penalty method. It is written by a penalty weight parameter λ^2 as

$$\min \left\| \hat{O}\hat{T} - C_2 \right\|_2^2 + \lambda^2 \left\| A\hat{T} - C_1 \right\|_2^2, \quad (20)$$

which is equivalent to

$$\min \left\| \hat{A}\hat{T} - \hat{C} \right\|_2^2 = \min \left\| \begin{array}{c} |\lambda| (A\hat{T} - C_1) \\ \hat{O}\hat{T} - C_2 \end{array} \right\|_2^2 \quad (21)$$

where $\hat{A} = (|\lambda|A, \hat{O})^T$, $\hat{T} = (T, Y)^T$ and $\hat{C} = (\lambda C_1, C_2)^T$.

As shown in Eq.(21), the constrained optimization problem of the TFI-HSS task is transformed into an unconstrained optimization problem. In real-life applications, observations are inevitably perturbed by noises. For the unconstrained optimization problem in Eq.(21), according to **Theorem 3.1**, we have proven that when observation C has a perturbation δC , the relative error of the TFI-HSS task has an upper bound, which is related to the condition number of \hat{A} . For

$$\hat{A} = \begin{pmatrix} \lambda A \\ \hat{O} \end{pmatrix}, \quad (22)$$

if boundary conditions and positions of components are confirmed, the matrix A can be uniquely determined. The matrix \hat{O} is determined by positions of observations. Choosing positions reasonably can find a matrix \hat{A} with a smaller condition number, which results in a smaller relative error upper bound of the TFI-HSS task. It is more possible to obtain a robust temperature field by the PINN-TFI method with these positions under the same number of noise observations. Therefore, the condition number of \hat{A} becomes the principle to evaluate positions of observations.

In a summary, the CMCN-PSO method can be briefly described as follows. Assume that there are L sets of positions $\{(x_1, y_1), \dots, (x_m, y_m)\}, \dots, \{(x_{Lm+1}, y_{Lm+1}), \dots, (x_{(L+1)m}, y_{(L+1)m})\}$. They can be converted to matrix form $\hat{O}_1, \dots, \hat{O}_L$. Then, according to Eq.(16), coefficient matrix A can be calculated. After that, combining O_1, \dots, O_L and A , the condition number κ_i , ($i = 1, \dots, L$) corresponding to different positions of observations O_i can be obtained. The minimal condition number is selected as the optimal condition number $\kappa_{optimal}$. Finally, the optimal positions $\hat{O}_{optimal}$ corresponding to $\kappa_{optimal}$ can be obtained. The optimal positions of observations is used for the PINN-TFI method can reconstruct a more robust temperature field.

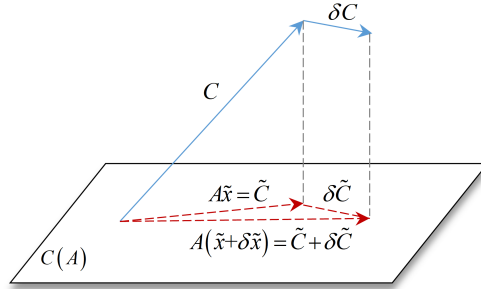


Figure 6: The diagram of the vectors.

Theorem 3.1 (Relative error upper bound). Suppose that A is m -by- n with $m > n$ and has full rank. Suppose that x minimizes $\|Ax - C\|_2$ and \tilde{x} is the solution. There is a perturbation δC in C . Let $x + \delta x$ minimize $\|A(x + \delta x) - (C + \delta C)\|_2$ and $\tilde{x} + \delta \tilde{x}$ is the solution. Then,

$$\frac{\|\delta \tilde{x}\|_2}{\|\tilde{x}\|_2} \leq \frac{\kappa(A)}{M} \frac{\|\delta C\|_2}{\|C\|_2}, \quad (23)$$

where $\kappa(A) = \|A\|_2 \left\| (A^H A)^{-1} A^H \right\|_2$ and M is a constant.

Sketch of Proof of Theorem 3.1.

The area $C(A)$ is shown in Fig. 6, which represents the column space of A . The vector C typically will not be in $C(A)$. \tilde{C} is the projection of C onto $C(A)$ and \tilde{x} takes the correct linear combinations of the matrix A to obtain \tilde{C} , which can be written as

$$\tilde{C} = A\tilde{x}. \quad (24)$$

If there is a change δC to C , there is a small change $\delta\tilde{C}$ in the projection of $C + \delta C$. Because projection is multiplication by the projection matrix, we can obtain

$$A(\tilde{x} + \delta\tilde{x}) = \tilde{C} + \delta\tilde{C}. \quad (25)$$

For

$$\cos \theta = \frac{\|\tilde{C}\|_2}{\|C\|_2}, \quad (26)$$

it can be written as

$$\cos \theta \|C\|_2 = \|\tilde{C}\|_2 = \|A\tilde{x}\|_2 \leq \|A\|_2 \|\tilde{x}\|_2. \quad (27)$$

Because $\delta\tilde{x}$ is equivalent to $A^\dagger \delta\tilde{C}$, $\|\delta\tilde{x}\|_2$ can be computed by

$$\|\delta\tilde{x}\|_2 = \|A^\dagger \delta\tilde{C}\|_2 \leq \|A^\dagger\|_2 \|\delta\tilde{C}\|_2, \quad (28)$$

where A^\dagger represents $(A^H A)^{-1} A^H$. Combing Eq.(27) and Eq.(28), the relative error can be formulated by

$$\begin{aligned} \frac{\|\delta\tilde{x}\|_2}{\|\tilde{x}\|_2} &\leq \frac{\|A\|_2 \|A^\dagger\|_2 \|\delta\tilde{C}\|_2 \|\delta C\|_2}{\cos \theta \|\delta C\|_2 \|\tilde{C}\|_2} \leq \kappa(A) \frac{\cos \tilde{\theta} \|\delta C\|_2}{\cos \theta \|\tilde{C}\|_2} \\ &\leq \frac{\kappa(A) \|\delta C\|_2}{M \|\tilde{C}\|_2}, \end{aligned} \quad (29)$$

where $\kappa(A)$ is equivalent to $\|A\|_2 \|(A^H A)^{-1} A^H\|_2$ and constant ($M > 0$) is equivalent to $\sup(\cos \theta)$.

4 Experiment

In this section, we mainly investigate the effectiveness performance of the PINN-TFI method and the CMCN-PSO method. Based on three typical cases, experiments are mainly to solve two tasks, namely TFI-HSS with noiseless observations and TFI-HSS with noise observations. (i) TFI-HSS with noiseless observations is designed to validate the effectiveness of the PINN-TFI method, where three sampling methods are used to select observations. (ii) For TFI-HSS with noise observations, the CMCN-PSO method is used to select positions of observations. Then, the PINN-TFI method is utilized to evaluate whether a more robust temperature field can be reconstructed with the optimal positions.

4.1 Experiment setups

Configurations of cases: In this section, three typical cases are introduced to test performances of the PINN-TFI method and the CMCN-PSO method for the TFI-HSS task. The two-dimensional plane is modeled a square domain with the size $10cm \times 10cm$. All cases with different boundaries are shown as follows.

For all the data (observations and exact temperature filed), FEniCS [Alnæs et al., 2015] is used to generate thermal simulation results.

- **Case 1:** VB problem with identical boundary conditions for four boundaries. All boundaries are isothermal with constant temperature valued 298K (see Fig. 7(a) for better understanding).
- **Case 2:** VB problem with different boundary conditions. The bottom boundary is isothermal with constant temperature valued 298K and other boundaries are adiabatic. Fig. 7(b) describes this type of VB problem.
- **Case 3:** VP problem with heat sink of width $1cm$. A finite heat-generating volume cooled by a small patch of the common heat sink with the temperature of 298K located on the middle of the bottom boundary. The rest boundaries are adiabatic. Fig. 7(c) shows this type of VP problem.

Three sampling methods: This work considers Latin hypercube sampling, low discrepancy sampling, and grid-based sampling to select observations. The main motivation is to generate sets of points, which can uniformly coverage of the space.

- Latin hypercube sampling (LHS) is to generate a quasi-random sampling distribution. Suppose n samples are sampled from the two-dimensional space. Each dimension is divided into n intervals that do not overlap each other, and each interval has the same probability (it usually considers a uniform distribution so that the interval length is the same). One point then is sampled from each interval in each dimension. Finally, we randomly extract the points sampled in the previous step from each dimension and compose them into a vector.

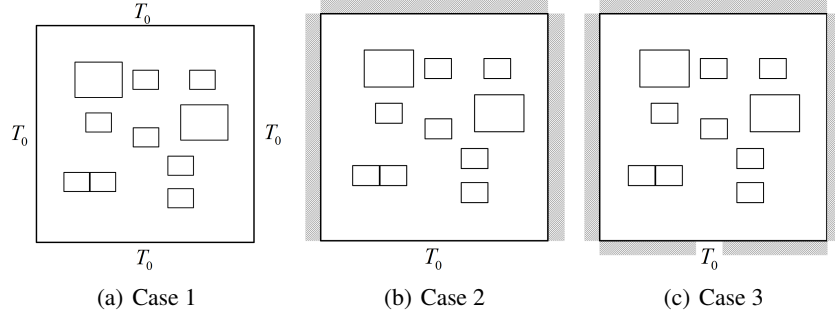


Figure 7: The illustration of VP and VB problem in a square domain.

- Low discrepancy sampling (LDS) is to generate the low discrepancy sequence. Assume that the point set X is sampled from the two-dimensional domain. Given a set $P = \{x_1, \dots, x_n\}$, the discrepancy of P is defined as follows:

$$\mathcal{D}(P) = \sup_{B \in \mathcal{J}} \left| \frac{\mathcal{C}(B, P)}{N} - \lambda(B) \right|, \quad (30)$$

where λ is the Lebesgue measurement of B , $\mathcal{C}(B, P)$ is the number of points in P that falls into B , and \mathcal{J} is the set of two-dimensional intervals. The purpose of the low-discrepancy sequence is to make the discrepancy of the resulting points as small as possible. The detailed method can refer to [Cervellera et al., 2014].

- Grid-based sampling (GS) is to select observations based on mesh points. The most used way is to place as many observations as possible at important positions (such as positions of components). Therefore, except for some pre-defined observations (positions of components and other positions placed by engineers), the whole domain is meshed as a $K \times K$ grid system, and observations are added through the grid to achieve the overall uniformity of observations. Concretely, one observation is placed at components (center positions of components in our work) and some observations are placed by engineers' experiences. Then, the two-dimensional domain is meshed as a $N \times N$ grid system to determine whether there are observations inside grid areas. If not, observations are placed inside the area (grid center position). In particular, when the pre-defined observations are located on the gridlines, the points are considered to belong to the upper-right grid.

Evaluation Metrics: This work uses four metrics to evaluate performances of the reconstructed temperature field as follows:

- **Mean Absolute Error (MAE).** MAE is the mean absolute error of the whole reconstructed temperature field, which can be written as

$$E_{MAE} = \frac{1}{N^2} \sum_{i=1}^N \sum_{j=1}^N |T_\theta(x_i, y_j) - T_s(x_i, y_j)|, \quad (31)$$

where $T_\theta(x_i, y_j)$ and $T_s(x_i, y_j)$ represent the predicted temperature and the ground-truth temperature by numerical simulations, respectively.

- **Component-constrained MAE (CMAE).** CMAE is defined to calculate the mean absolute error of the area that heat sources cover, which can be formulated as

$$E_{CMAE} = \frac{1}{|\Omega_{com}|} \sum_{(x_i, y_j) \in \Omega_{com}} |T_\theta(x_i, y_j) - T_s(x_i, y_j)|, \quad (32)$$

where Ω_{com} represents the area of heat sources cover.

- **Boundary-constrained MAE (BMAE).** BMAE is defined to calculate the mean absolute error of the boundary area, which can be calculated as

$$E_{BMAE} = \frac{1}{|\Omega_b|} \sum_{(x_i, y_j) \in \Omega_b} |T_\theta(x_i, y_j) - T_s(x_i, y_j)|, \quad (33)$$

where Ω_b represents the boundary area.

- **Maximum of Component-constrained Absolute Error (M-CAE).** M-CAE is defined to calculate the maximum error of the temperature field, which be computed as

$$E_{M-CAE} = \max_{(x_i, y_j) \in \Omega} |T_\theta(x_i, y_j) - T_s(x_i, y_j)|, \quad (34)$$

where Ω_{com} represents the whole domain.

Optimization and hyperparameters: By default, Adam solver [Kingma and Ba, 2014] is used with an initial learning rate of $1e-3$. Four hidden layers with 50 neurons in each layer are used. The weights w_{PDE} , w_{BC} and w_{data} are set to 1, 1, and $1e4$, respectively. The training iteration is set to be 5,000.

Compute Infrastructure: A very common machine with a 2.8-GHz Intel(R) Xeon(R) Gold 6242 CPU, 128-GB memory, and NVIDIA GeForce RTX 3090 GPU was used to test the performance of proposed methods.

All implementations for the TFI-HSS task are based on an open source deep learning framework Pytorch.

4.2 TFI-HSS with noiseless observations

To investigate the effectiveness of the PINN-TFI method, we first consider solving the TFI-HSS task with noiseless observations. Three sampling methods are used to generate positions of observations. Following we mainly present the performance of the PINN-TFI method with the different number of observations, the performance of the PINN-TFI method with and without transfer strategy, the performance of the PINN-TFI method with different width and depth of the NN, the performance of the PINN-TFI method with different weights, and the comparisons with other methods.

4.2.1 Performance with the different number of observations

In this part, we conduct experiments under different numbers of observations from Latin hypercube sampling (LHS), low discrepancy sampling (LDS) and grid-based sampling (GS). The number of observations is chosen from $\{42, 68, 104, 148\}$. Fig. 8 shows positions and intensities of components as well as true temperature fields for three cases.

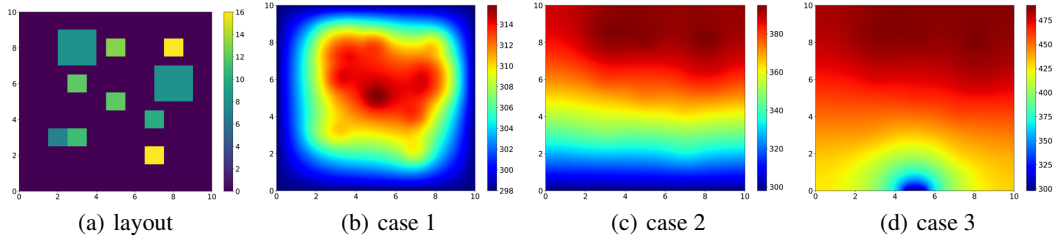


Figure 8: The component layout and true temperature fields for three cases.

Table 1 lists the performance of the PINN-TFI method with 42, 68, 104, and 148 observations, where LHS, LDS, and GS are used to generate positions of observations. MAEs over three cases are decreasing with the increase of

Table 1: Performance of the PINN-TFI method with different numbers of observations from Latin hypercube sampling (LHS), low discrepancy sampling (LDS) and grid-based sampling (GS). The best results under different numbers of observations are highlight.

Num	Position	Case 1				Case 2				Case 3			
		MAE	CMAE	BMAE	M-CAE	MAE	CMAE	BMAE	M-CAE	MAE	CMAE	BMAE	M-CAE
42	LHS	0.3515	0.4588	0.1545	2.1604	0.7120	0.4889	0.8295	2.7160	0.8488	0.5006	2.0459	2.2240
	LDS	0.3058	0.2804	0.1249	1.7357	0.5353	0.3821	0.5939	2.2917	0.7587	0.4689	1.2950	1.8336
	GS	0.4396	0.3287	0.2531	2.1168	0.6817	0.3958	0.5664	1.6842	0.6488	0.3809	1.3150	1.7395
68	LHS	0.1946	0.1345	0.1272	0.9913	0.2956	0.3047	0.6487	1.0054	0.3794	0.3504	0.9033	1.5122
	LDS	0.1938	0.1446	0.1245	0.8330	0.2859	0.2564	0.5440	0.8572	0.4078	0.3471	1.2371	1.4958
	GS	0.1816	0.1109	0.1892	0.7215	0.2472	0.1913	0.5506	0.9930	0.4262	0.2573	1.1508	1.4526
104	LHS	0.1789	0.1976	0.1097	1.2450	0.2201	0.1760	0.3241	0.9592	0.4490	0.4701	1.6813	1.3689
	LDS	0.1127	0.1178	0.1250	0.6170	0.1850	0.2151	0.2111	1.1666	0.2927	0.2825	0.7925	1.4032
	GS	0.1785	0.1214	0.1961	0.6443	0.2163	0.1675	0.4997	0.8172	0.2833	0.2230	0.9241	0.7633
148	LHS	0.1157	0.0934	0.1207	0.5232	0.2309	0.1449	0.4662	0.9938	0.3823	0.3942	1.2509	1.7600
	LDS	0.0904	0.1138	0.0924	0.7660	0.1275	0.1652	0.1545	0.6356	0.2562	0.3160	0.6972	1.0443
	GS	0.0918	0.0693	0.1896	0.3086	0.1070	0.1095	0.2512	0.6675	0.2115	0.2750	0.8019	1.1034

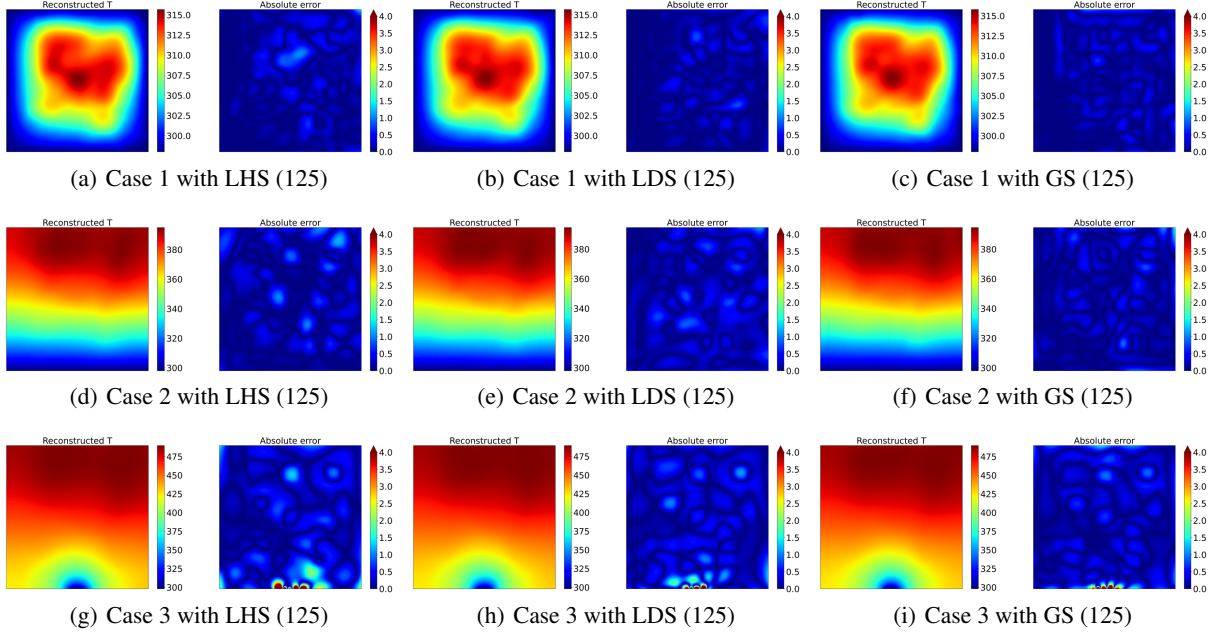


Figure 9: Examples of the PINN-TFI method with 125 observations for TFI-HSS task.

observations and are less than 0.5K under just 42 observations. CMAEs and the BMAEs are also less than 0.6K under just 42 observations. The prediction accuracy is acceptable even when the number of observations is extremely small. This also indicates the PINN-TFI method can work well in a small data setting. Except for case 3 with 68 observations, LDS and GS can find better positions for the PINN-TFI method to achieve smaller errors than LHS under the same number of observations. For case 1, the performance of the PINN-TFI method with 42 and 148 observations from LDS is better than that from GS. Fig. 9 shows the examples of the PINN-TFI method with 125 observations from LHS, LDS, and GS, respectively.

It is more intuitive to get the above conclusion from Fig. 10. As the figure shows, LDS and GS are better than LHS. The trends of MAEs of the PINN-TFI method with observations from LDS and GS are close. The MAEs of LDS and GS are decreasing with the increase of observations except for case 2 under 125 observations. Obviously, when the number of observations differs greatly, the performance of the PINN-TFI method with more observations is better than fewer ones whatever observations are from LHS, LDS, or GS. But when the number of observations is close, the performance of the PINN-TFI method with more observations from LHS might not be better than fewer ones. It also can be seen that when the number of observations increases to some level, the performance improves slightly.

4.2.2 Performance with and without transfer learning strategy

To use transfer learning strategy for the acceleration, the PINN-TFI method designs the model initialization part, where observations are not required. Transfer learning strategy is used to initialize the NN model. In addition, Xavier initialization is a widespread initialization method used by many works [Raissi et al., 2019, 2020]. To show the acceleration effect, this work compares the performance of the PINN-TFI method with transfer learning strategy and Xavier initialization.

Fig. 11 shows the performance of the PINN-TFI method over three cases with transfer learning and Xavier initialization under 5 000 iterations. MAEs, CMAEs, BMAEs, and M-CAEs of the PINN-TFI method with transfer learning are significantly less than that of the PINN-TFI method with Xavier initialization whatever observations are from LHS, LDS, or GS. For three cases, MAEs, CMAEs, BMAEs, and M-CAEs of the PINN-TFI method with Xavier initialization are close whatever observations are from LHS, LDS, or GS. Fig. 12 shows the historical MAEs of the PINN-TFI method over three cases with transfer learning and Xavier initialization. More obviously, the curves of MAEs with Xavier initialization are almost close for observations from LHS, LDS, and GS. It means that, in the early stage of the training process, positions of observations have little influence on the NN with Xavier initialization. For observations from LHS, LDS, and GS, curves of MAEs with transfer learning are close within about 100 iterations. The curves of MAEs with transfer learning are going down very fast and MAEs with transfer learning converge to different values.

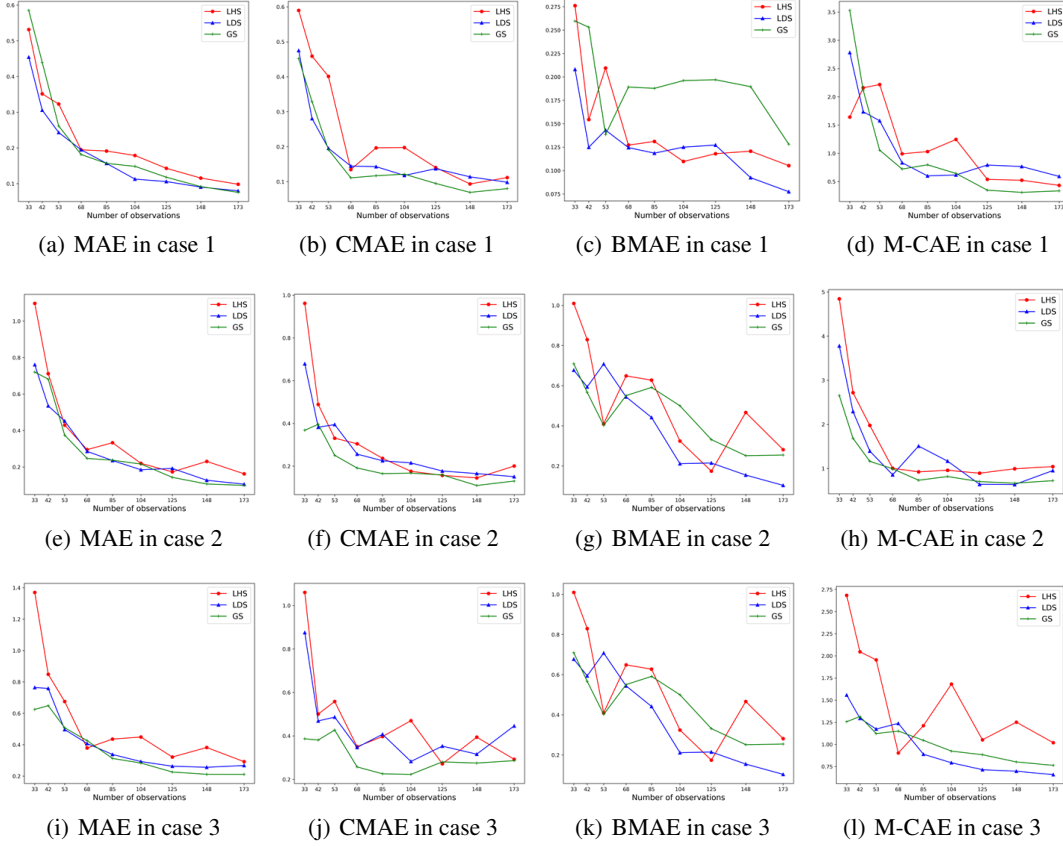


Figure 10: Performance of the PINN-TFI method with different number of observations.

Transfer learning strategy has embedded physical informations learned in the model initialization part into the model for temperature field inversion. It means that transfer learning strategy endows the model for temperature field inversion with a good start, which makes the model efficiently learning from observations.

4.2.3 Performance with different width and depth of the NN

We conduct experiments with different NN architectures. The NN 1 has four hidden layers with 50 neurons in each layer, which is the default NN architecture setting in this work. The NN 2 has four layers with 100 neurons in each layer. The NN 3 has five layers with 50 neurons in each layer and the NN 4 has three layers with 50 neurons in each layer.

Table 2: Performance of the PINN-TFI method with observations from LHS, LDS, and GS under different widths and depths of NNs. The best results under different NN architectures are highlight.

NN	Position	Case 1				Case 2				Case 3			
		MAE	CMAE	BMAE	M-CAE	MAE	CMAE	BMAE	M-CAE	MAE	CMAE	BMAE	M-CAE
NN 1	LHS	0.1430	0.1404	0.1180	0.5387	0.1736	0.1569	0.1740	0.8939	0.3216	0.2714	1.0518	1.622
	LDS	0.1059	0.1370	0.1272	0.7929	0.1924	0.1772	0.2146	0.6410	0.2631	0.353	0.7143	1.1276
	GS	0.1181	0.0948	0.1970	0.3472	0.1434	0.1589	0.3312	0.7032	0.2261	0.2806	0.8834	0.9634
NN 2	LHS	0.2179	0.2179	0.2178	0.9259	0.1973	0.1838	0.2687	0.9562	1.1225	0.5746	5.2919	2.1522
	LDS	0.1165	0.0959	0.0882	0.5925	0.1988	0.1826	0.2062	0.8449	0.4194	0.4402	1.7399	1.5644
	GS	0.1368	0.0952	0.1981	0.5274	0.1696	0.0957	0.3098	0.6655	0.4894	0.3042	2.3088	1.7257
NN 3	LHS	0.1551	0.1540	0.1788	0.7427	0.1883	0.1528	0.3366	0.9703	1.2614	1.0379	5.0108	2.4625
	LDS	0.1196	0.1424	0.1933	0.8760	0.3859	0.4776	0.3539	1.3347	0.5327	0.8412	1.7858	2.1799
	GS	0.1242	0.1083	0.2176	0.5793	0.1644	0.1242	0.3532	0.7579	0.5695	0.7951	1.9217	1.7909
NN 4	LHS	0.1542	0.1543	0.1176	1.0330	0.1989	0.1699	0.3240	1.0549	0.8812	0.5461	3.7753	3.6405
	LDS	0.1245	0.1610	0.1165	0.8282	0.2023	0.2661	0.2434	0.8543	0.7641	0.6060	2.0173	2.0880
	GS	0.1284	0.1141	0.2410	0.5655	0.1657	0.1300	0.3516	0.6657	0.4380	0.4266	2.1595	2.0787

Table 2 shows the performance of the PINN-TFI method with different NN architectures, where the best results of MAEs, CMAEs, BMAEs, and M-CAEs can be obtained by NN 1 (default NN architecture) except for the BMAE of

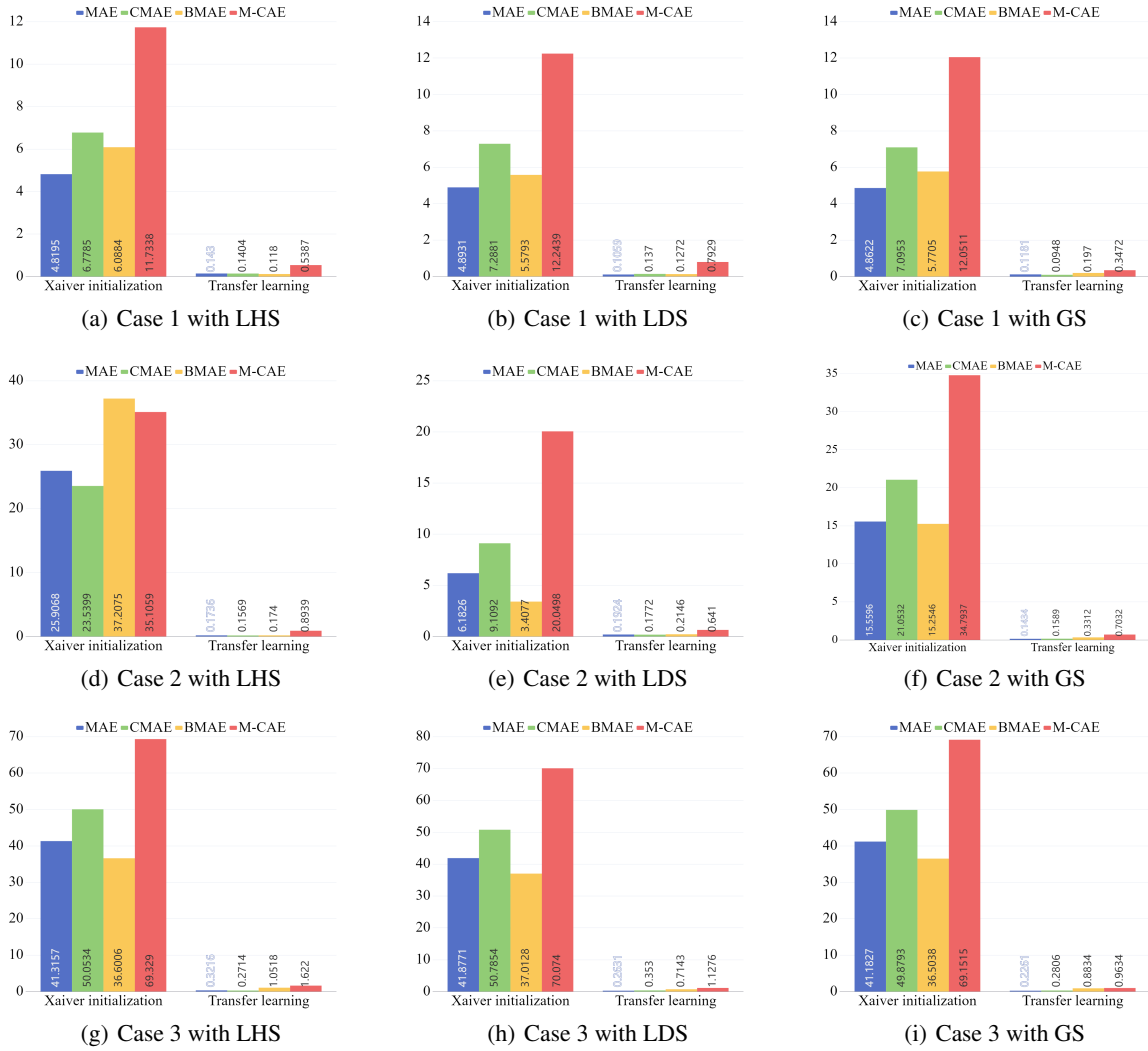


Figure 11: Performance of the PINN-TFI method with Xavier initialization and transfer learning.

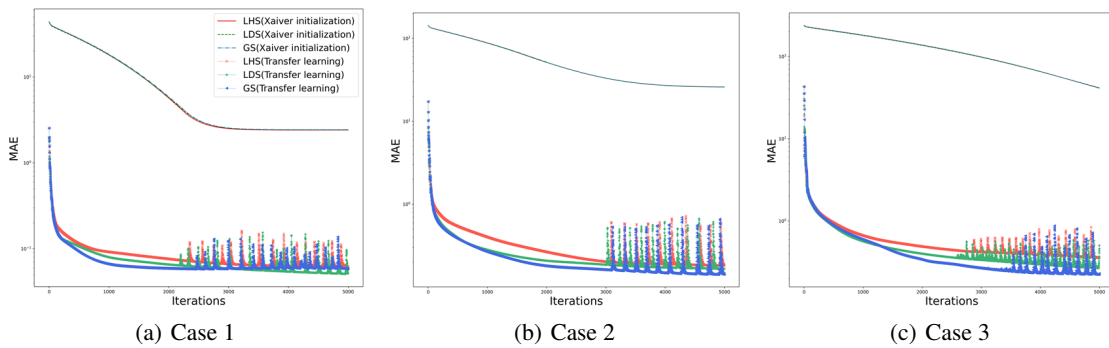


Figure 12: The historical MAE of PINN-TFI method over three cases with transfer learning and Xavier initialization.

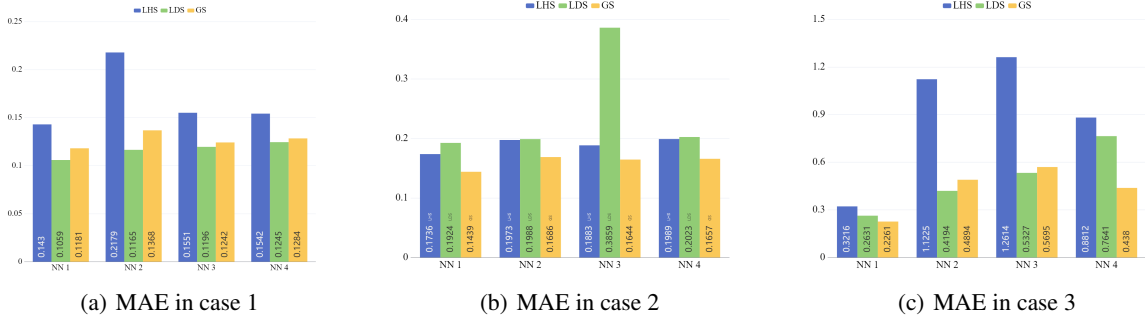


Figure 13: MAEs of the PINN-TFI method with observations from LHS, LDS, and GS under different NNs.

case 1 and the CMAE of case 2. Compared to NN 1, NN 2 has the same depth but has more neurons in each layer. As Fig. 13 shows, MAEs of the PINN-TFI method with NN 2 are larger than ones with NN 1. For NN1 and NN3, the more neurons in the hidden, the larger MAEs. Additionally, the MAE of the PINN-TFI method with NN 3 over case 3 tends to be 1.2614K, which is significantly larger than 0.3216K with NN 1. It means that an unusually large number of neurons in the hidden layers will cause overfitting. Compared to NN 1, NN 4 has the same number of neurons in each layer but has the less depth. MAEs of the PINN-TFI method with NN 4 is worse than ones with NN 1. It means that a shallow NN architecture can not learn enough physics information to depict the whole temperature field. In a summary, a NN architecture of appropriate width and depth enable the PINN-TFI method to achieve better performance.

4.2.4 Performance with different weights

To encode physics and observation informations into the loss function, the PINN-TFI method constructs three different losses, namely the PDE loss, BC loss, and Data loss. Three losses are combined with weights, which play different roles in the training process. This work designs different weights to discuss the effect of different losses. The default weight setting ($w_{pde} = 1$, $w_{bc} = 1$ and $w_{data} = 1e4$) is used the baseline of the comparison.

Fig. 14 also shows the performance of the PINN-TFI method under different weights. As figure shows, compared with weight 1, weight 4 decreases w_{bc} . Thus, BMAEs under weight 4 are significantly less than that under weight 1. But a larger w_{bc} causes a slight increment in MAEs. BC loss plays an important role for BMAEs. MAEs under weight 5 are larger than that under weight 1. This indicates that large w_{pde} is not suitable for the PINN-TFI method. In addition, for different observations from LHS, LDS, and GS, the influence of those different weight terms are close.

Table 3 lists results of the PINN-TFI method with observations from LHS, LDS, and GS under different weights. From the table, except for BMAEs, the best results of MAEs, CMAEs, and M-CAE can be obtained under weight 1. For weight 2, MAEs over three cases with GS tend to be 0.1181K, 0.1434K, and 0.2261K, which are less than 0.1287K, 0.1916K and 0.3524K with GS, respectively. This means that larger w_{data} increases the proportion of data loss in the total loss, which results in smaller MAEs. But it can be seen from results under weight 1 and weight 3 that an unusually large w_{data} may result in worse MAEs. Additional, larger w_{data} will also reduce the proportion of BC loss in the total loss, causing worse BMAEs for the PINN-TFI method. In conclusion, Data loss has a great influence on MAEs of the PINN-TFI method.

4.2.5 Comparisons with other methods

This work uses Gaussian process regression (GPR) [Schulz et al., 2018] and random forest regression (RFR) [Segal, 2004] as baselines, which are implemented with Sklearn toolbox [Pedregosa et al., 2011] (a very powerful machine learning Python library). It should be noted that all the results are obtained by calculating the average value of five independent repeated runs of the training. Fig. 15 shows the comparison result of these former methods with 42 observations after five independent repeated runs. For three cases, whatever observations are sampled from LHS, LDS, or GS, the PINN-TFI method outperforms GPR and RFR. The PINN-TFI method with 42 observations from LHS can obtain MAEs of 0.2883K, 0.6735K and 0.7735K over three cases. For observations from LDS, the PINN-TFI method obtains MAEs of 0.3538K, 0.5787K, and 0.7132K over three cases. For observations from GS, the PINN-TFI method obtains MAEs of 0.3538K, 0.5787K, and 0.7132K over three cases. Under the same observations, MAEs of GPR and RFR over three cases exceed 1.5K, 2K, and 4.5K, respectively. For different cases, performances of GPR and RFR change dramatically. Especially for the most complicated case 3, B-MAEs and M-CAEs of GPR and RFR exceed 10, which are far more than that of the PINN-TFI method. In addition, similar performances of the PINN-TFI method under

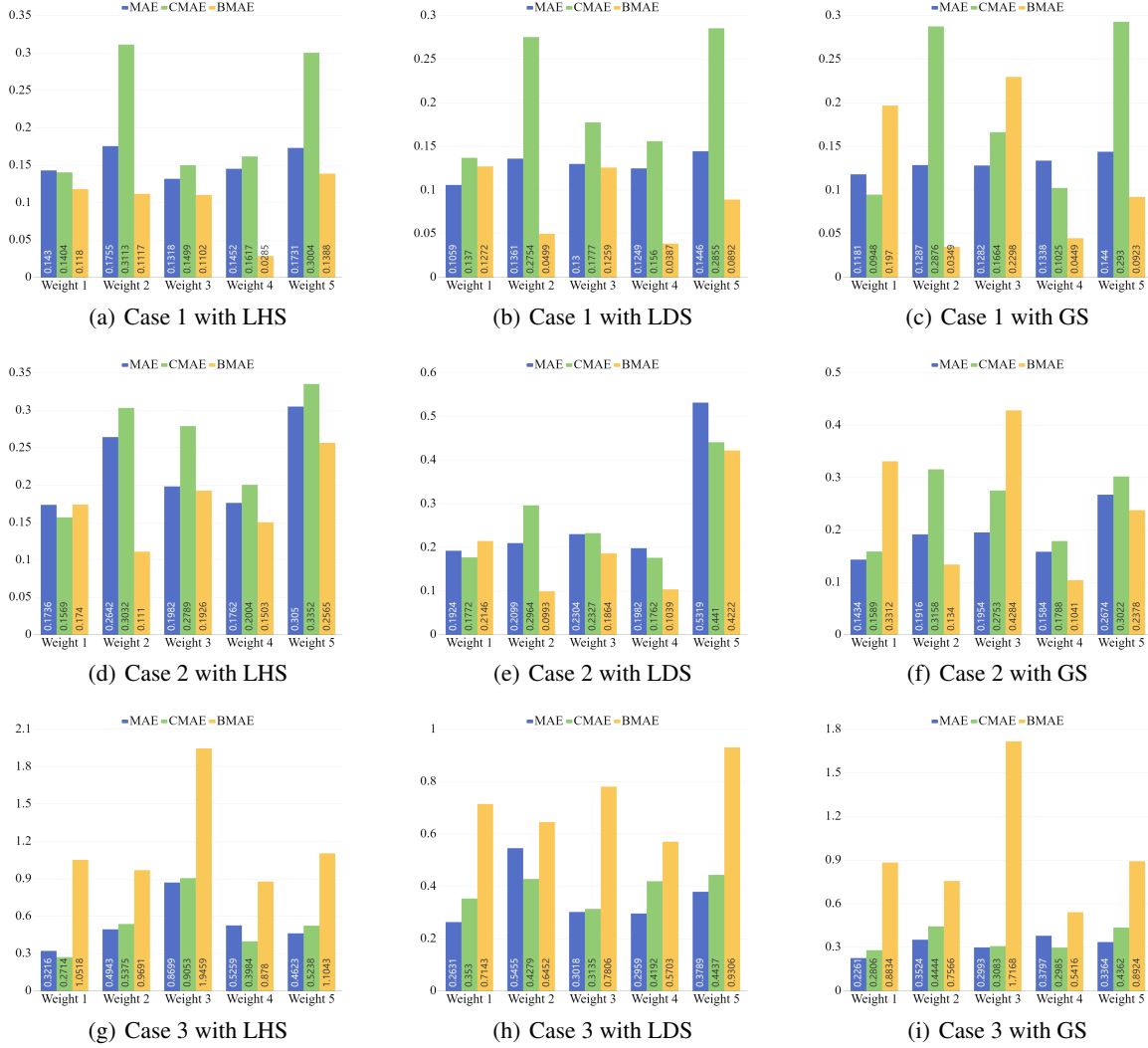


Figure 14: Performance of the PINN-TFI method with observations from LHS, LDS and GS under different weights.

Table 3: Performance of the PINN-TFI method with observations from LHS, LDS, and GS under different weights. The best results under different weights are highlight.

Weight	Position	Case 1				Case 2				Case 3			
		MAE	CMAE	BMAE	M-CAE	MAE	CMAE	BMAE	M-CAE	MAE	CMAE	BMAE	M-CAE
1	$w_{PDE}=1$ LHS	0.1430	0.1404	0.1180	0.5387	0.1736	0.1569	0.1740	0.8939	0.3216	0.2714	1.0518	1.6220
	$w_{BC}=1$ LDS	0.1059	0.1370	0.1272	0.7929	0.1924	0.1772	0.2146	0.6410	0.2631	0.3530	0.7143	1.1276
	$w_{BC}=1e4$ GS	0.1181	0.0948	0.1970	0.3472	0.1434	0.1589	0.3312	0.7032	0.2261	0.2806	0.8834	0.9634
2	$w_{PDE}=1$ LHS	0.1755	0.3113	0.1117	1.2655	0.2642	0.3032	0.1010	1.2645	0.4943	0.5375	0.9691	1.9090
	$w_{BC}=1$ LDS	0.1361	0.2754	0.0499	0.9108	0.2099	0.2964	0.0993	1.1959	0.5455	0.4279	0.6452	1.2501
	$w_{BC}=1e2$ GS	0.1287	0.2876	0.0349	0.9756	0.1916	0.3158	0.1340	1.1443	0.3524	0.4444	0.7566	1.3431
3	$w_{PDE}=1$ LHS	0.1318	0.1499	0.1102	1.1359	0.1982	0.2789	0.1926	1.1940	0.8699	0.9053	1.9459	1.8760
	$w_{BC}=1$ LDS	0.1300	0.1777	0.1259	0.7719	0.2304	0.2327	0.1864	1.3967	0.3018	0.3135	0.7806	1.1607
	$w_{BC}=1e6$ GS	0.1282	0.1664	0.2298	0.7088	0.1954	0.2753	0.4284	1.3503	0.2993	0.3083	1.7168	1.0400
4	$w_{PDE}=1$ LHS	0.1452	0.1617	0.0285	0.6933	0.1762	0.2004	0.1503	1.1180	0.4259	0.3984	0.8780	1.4880
	$w_{BC}=1e2$ LDS	0.1249	0.1560	0.0387	0.8034	0.1982	0.1762	0.1039	0.6677	0.2959	0.4192	0.5703	1.2571
	$w_{BC}=1e4$ GS	0.1338	0.1025	0.0449	0.3589	0.1584	0.1788	0.1041	0.7521	0.3797	0.2985	0.5416	1.1146
5	$w_{PDE}=1e2$ LHS	0.1731	0.3004	0.1388	1.1978	0.3050	0.3352	0.2565	1.3302	0.4623	0.5238	1.1043	1.6181
	$w_{BC}=1$ LDS	0.1446	0.2855	0.0892	0.8776	0.5319	0.4410	0.4222	0.9733	0.3789	0.4437	0.9306	1.4719
	$w_{BC}=1e4$ GS	0.1440	0.2930	0.0923	1.0036	0.2674	0.3022	0.2378	0.9963	0.3364	0.4362	0.8924	1.4793

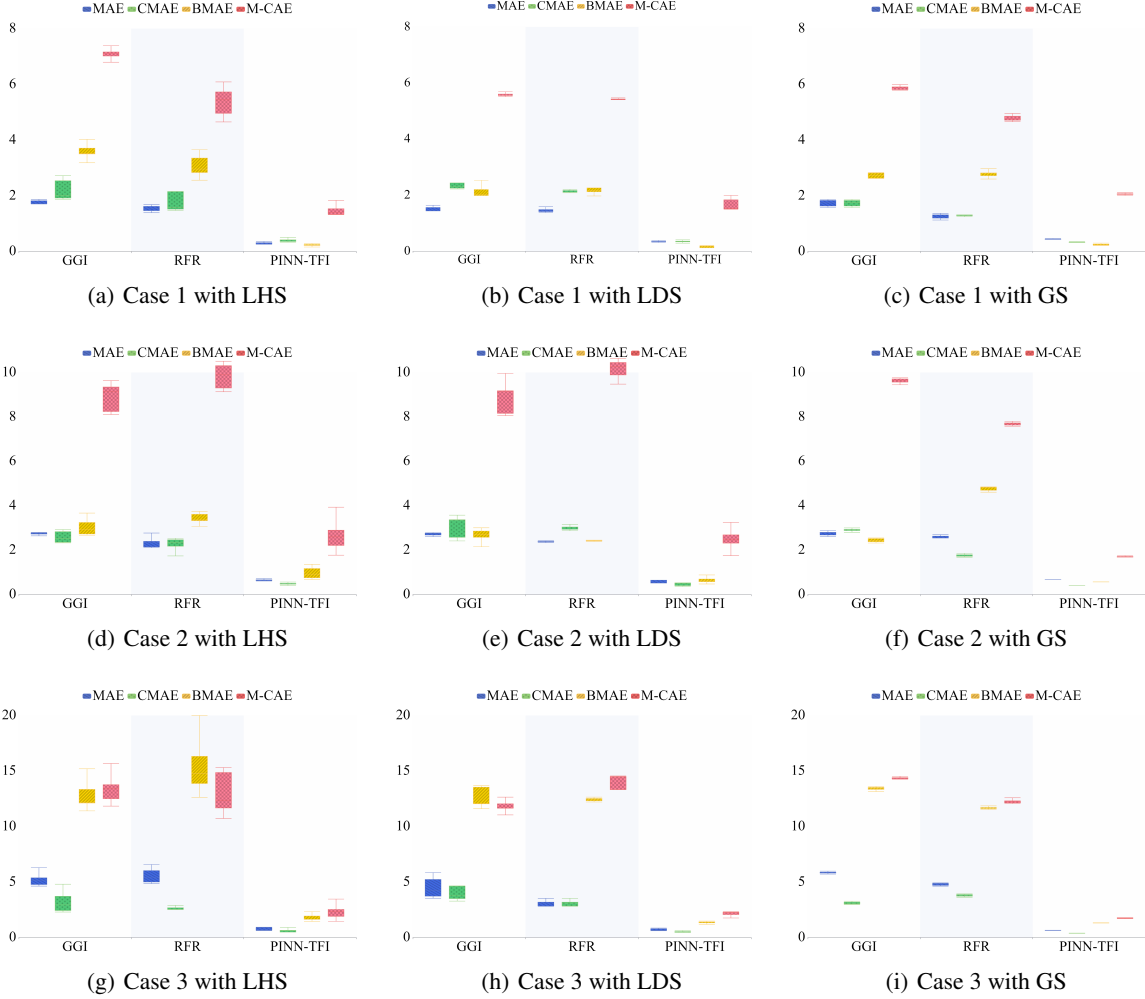


Figure 15: Performance of the PINN-TFI method, Gaussian process regression (GPR), and random forest regression (RFR) with 42 observations obtained from LHS, LDS and GS.

repeated runs indicate that the PINN-TFI method is more stable than GPR and RFR. In a word, the PINN-TFI method has a better reconstructed performance and is more suitable for the TFI-HSS task.

4.3 TFI-HSS with noise observations

To investigate the effectiveness of the CMCN-PSO method, this work first finds the optimal positions of noise observations and then uses them by the PINN-TFI method to solve the TFI-HSS task with noise observations. Concretely, we assume that there are 150 sets of positions under the same number of observations, where 50 sets are sampled from LHS, 50 sets are sampled from LDS, and 50 set is sampled from GS. The CMCN-PSO method is used to find the optimal positions and the PINN-TFI method with those noise observations is used to reconstruct the temperature field. Following we mainly present optimal positions of CMCN-PSO method with the different number of noise observations, the performance of the CMCN-PSO method with the different number of noise observations and the performance of the CMCN-PSO method with different noise levels.

4.3.1 Optimal positions of CMCN-PSO method with the different number of noise observations

This work ranks 50 sets of positions from LHS and LDS, respectively. The CMCN-PSO method is used to find the optimal set of positions and the PINN-TFI method uses optimal positions to reconstruct the temperature field. In the CMCN-PSO method, the two-dimensional domain is meshed as a 50×50 grid. To study the effect of additive noise in

observations, this work creates noise observations from the true data as follows:

$$T_{obs}^{noise} = T_{obs}^{true} + \epsilon T_{obs}^{true} \mathcal{G}(0, 1), \quad (35)$$

where T_{obs}^{noise} and T_{obs}^{true} represent observations with and without noises, respectively. The ϵ determines the noise level and $\mathcal{G}(0, 1)$ is a random value sampled from the Gaussian distribution with mean and standard deviation of 0 and 1. Sets of positions randomly sampled from LHS and LDS are used as baselines.

Table 4 shows the optimal set of positions with the CMCN-PSO method under the different number. The condition number of optimal positions is much smaller than that of positions from LHS and LDS. For three cases, optimal positions are different under 42 and 68 observations but are the same under 104 and 125 observations. It can be seen that the more the number of observations, the less boundary conditions affect positions of observations. It also means that when the number of observations is large enough, optima positions under different boundaries are the same. In addition, as boundary conditions of case 2 and case 3 are similar, the condition numbers obtained are also relatively close. Fig. 16 shows the optimal positions under different number of observations. For 42 observations, the number of observations is relatively small and the distribution of observations is mainly concentrated on components and boundaries. For 125 observations, the number of observations is relatively large, and observations are distributed around the components, on the components, and on the boundary.

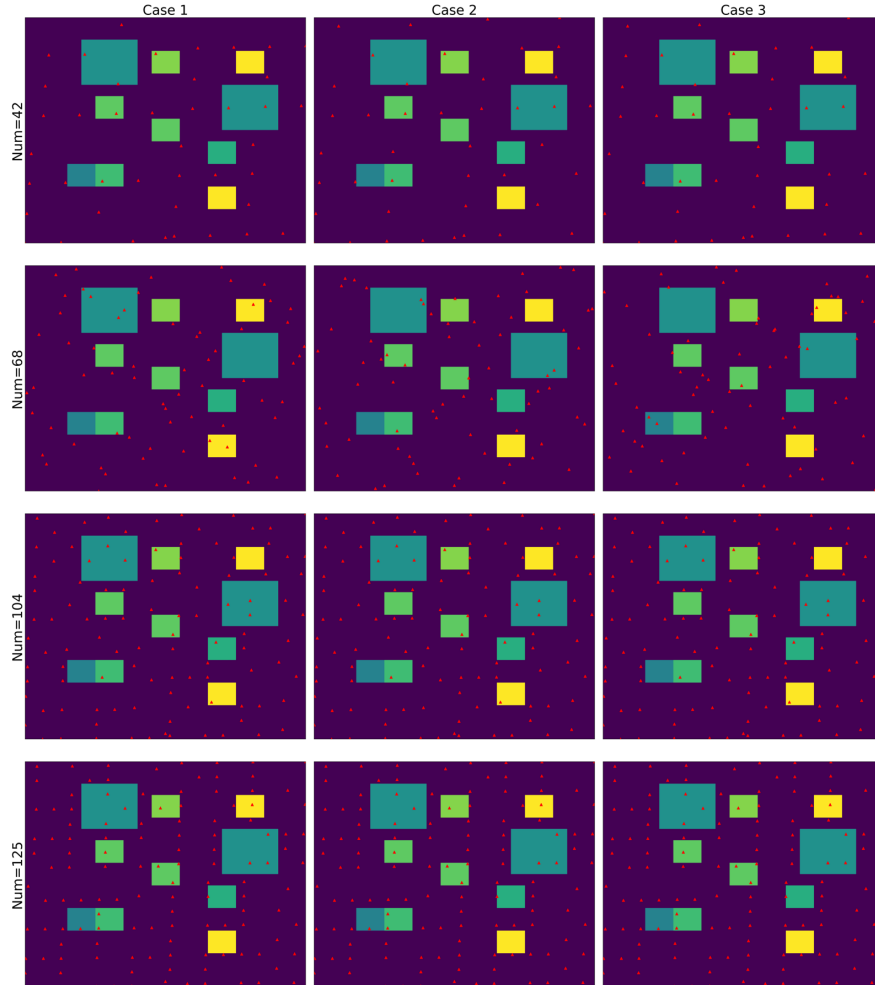


Figure 16: The optimal positions under different number of observations by the CMCN-PSO method.

4.3.2 Performance of the CMCN-PSO method with the different number of noise observations

To validate the effectiveness of optimal positions under the different number of observations, this work uses optimal positions to reconstruct the temperature field by the PINN-TFI method. The noise level ϵ is set to be 1%. Two sets of positions randomly sampled from LHS and LDS are used as baselines.

Table 4: The optimal set of positions with the CMCN-PSO method under different number of observations.

Num	Method	Case 1		Case 2		Case 3	
		position	condition number	position	condition number	position	condition number
42	CMCN-PSO	45(LDS)	154.7281	23(LDS)	154.3268	18(LDS)	158.3182
	LHS	-	250.8578	-	332.8663	-	265.5762
	LDS	-	201.7295	-	245.5780	-	259.9114
68	CMCN-PSO	0(LHS)	128.7127	37(LHS)	135.1052	13(LHS)	138.1758
	LHS	-	224.8941	-	226.2464	-	267.6193
	LDS	-	166.6221	-	169.4719	-	241.2854
104	CMCN-PSO	5(LDS)	85.5572	5(LDS)	86.0331	5(LDS)	86.0380
	LHS	-	165.8742	-	167.8742	-	150.0379
	LDS	-	158.8168	-	142.2804	-	127.8972
125	CMCN-PSO	7(LDS)	84.1118	7(LDS)	84.6107	7(LDS)	84.6015
	LHS	-	140.2223	-	130.2663	-	133.6214
	LDS	-	129.6307	-	131.3137	-	122.4524866

Table 5 shows the performance of optimal positions of the CMCN-PSO method and positions from LHS and LDS under the different number of observations when $\epsilon = 1\%$. For three cases, MAE and BMAE of the CMCN-PSO method are the smallest under the same number. For CMAE and M-CAE, the CMCN-PSO method can obtain minimum values in most instances. In addition, for 104 and 125 observations, four evaluation metrics of the CMCN-PSO method are best. When observations are perturbed by noises, as expected, the more the number of observations, the better reconstruction performance of the temperature field. Under 42 observations, the MAE of CMCN-PSO for case 1 is around 0.1K smaller than that of LHS, and MAEs of the CMCN-PSO method for case 2 and case 3 are around 0.5K and 0.4K smaller than that of LHS, respectively. This also indicates that the CMCN-PSO method might alleviate the effect of noises more significantly for more complex boundaries.

Table 5: Performance of the optimal positions of the CMCN-PSO method and positions from LHS and LDS under different number of observations when $\epsilon = 0.01$. The best results under different numbers are highlight.

Num	Method	Case 1				Case 2				Case 3			
		MAE	CMAE	BMAE	M-CAE	MAE	CMAE	BMAE	M-CAE	MAE	CMAE	BMAE	M-CAE
42	CMCN-PSO	0.8849	0.9684	0.8132	3.0784	1.2722	1.3888	1.1286	4.5438	2.2899	1.8989	3.336	6.3405
	LHS	0.9861	1.1839	1.2454	3.20171	1.7742	2.0686	1.6654	5.4797	2.6843	2.6879	4.0735	9.4054
	LDS	0.9064	0.9611	1.0361	3.0813	1.3412	1.5411	1.9054	3.9012	2.4882	2.6626	4.1432	8.1555
68	CMCN-PSO	0.7057	0.8385	0.6280	3.2573	1.0757	1.4777	1.2119	3.0310	2.0185	1.5687	3.0101	4.7467
	LHS	0.9227	1.0771	0.7690	3.2407	1.3559	1.0771	2.4239	3.1023	2.4958	1.8365	5.3349	5.6113
	LDS	0.8946	0.9381	0.8918	3.4484	1.2111	1.3066	1.6656	3.4262	2.385	1.6333	2.7971	6.5685
104	CMCN-PSO	0.6502	0.5978	0.6270	1.6969	0.8929	0.8374	1.1587	2.5145	1.3054	1.3568	1.6258	3.7029
	LHS	0.8604	0.8682	1.0192	3.4401	1.3010	0.9180	1.7530	3.1858	1.8954	1.5200	3.6248	4.0593
	LDS	0.8577	0.7621	0.9487	3.1495	1.1517	1.0744	1.3964	3.6843	1.7339	1.5567	2.402	4.9645
125	CMCN-PSO	0.5871	0.4700	0.7871	1.8628	0.7891	0.8074	1.0721	2.1150	1.1694	1.0035	2.0039	3.1011
	LHS	0.7888	0.4846	0.9219	2.5283	1.2531	1.1884	1.7325	4.1278	1.6627	1.2016	3.3963	3.8837
	LDS	0.7011	0.6131	0.9556	2.4351	1.1676	1.0332	1.2427	4.9933	1.6328	1.6830	2.2841	5.2096

4.3.3 Performance with different noise levels

This experiment is designed to validate the effectiveness of the CMCN-PSO method under various noise levels. The number of observations is set to be 68. The noise level ϵ is chosen from $\{0.25\%, 0.5\%, 1\%, 2\%\}$. Two sets of positions randomly sampled from LHS and LDS are used as baselines.

Table 6 shows the performance of optimal positions by the CMCN-PSO method and positions from LHS and LDS under different noise levels. Except for case 1 under the 1% noise level, MAEs of the CMCN-PSO method are best. The best MAE for case 1 under the 1% noise level tends to be 0.3908K, which is very close to 0.7057K by the CMCN-PSO method. It means that the CMCN-PSO method at different noise levels can achieve superior performance. As expected, the table shows that the predicted accuracy decreases as noise levels go up. Especially for case 3 under the 2% noise level, M-CAEs of LHS and LDS tend to be 16.1207K and 13.206K, which means a large noise level can cause a very terrible maximum error. But, the CMCN-PSO method can reduce the M-CAE to 7.8713K, which indicates that reasonable position selection can reduce the maximum error to a certain extent.

5 Conclusions

In this paper, the TFI-HSS task is defined by giving the formula expression. Then, we further develop a physics-informed neural network-based temperature field inversion (PINN-TFI) method and a coefficient matrix condition number based position selection of observations (CMCN-PSO) method. To solve the TFI-HSS task with limited observations, the PINN-TFI method firstly encodes physics and data constrains terms into the loss function. Then, the problem of

Table 6: Performance of optimal positions by the CMCN-PSO method and positions from LHS and LDS under different noise level when the number of observations is equal to 68. The best results under different numbers are highlight.

ϵ	Method	Case 1				Case 2				Case 3			
		MAE	CMAE	BMAE	M-CAE	MAE	CMAE	BMAE	M-CAE	MAE	CMAE	BMAE	M-CAE
0.25%	CMCN-PSO	0.2814	0.2437	0.2669	1.2041	0.3792	0.3258	0.6133	1.4276	0.4632	0.3642	1.0145	1.4645
	LHS	0.3307	0.4341	0.3298	1.3273	0.6474	0.5319	0.7124	1.9306	0.8011	0.7824	1.5316	2.3995
	LDS	0.2975	0.3523	0.2433	1.0332	0.4098	0.2934	0.7878	1.1030	0.6871	0.5647	1.4279	1.6981
0.5%	CMCN-PSO	0.4027	0.3991	0.3262	1.5099	0.5471	0.5348	0.6267	1.8197	0.7231	0.5639	1.4998	1.7774
	LHS	0.4911	0.6706	0.4566	2.1253	1.1086	1.0223	1.6337	3.4122	1.4456	1.5260	2.1647	4.8312
	LDS	0.3908	0.3447	0.4023	1.9413	0.5611	0.4383	0.9114	1.7046	0.8014	0.7939	1.3544	3.2351
1%	CMCN-PSO	0.7057	0.8385	0.6282	3.2573	1.0757	1.4777	1.2119	3.0310	2.0185	1.5687	3.0101	4.7467
	LHS	0.9227	1.0771	0.7691	3.2407	1.3559	1.0771	2.4239	3.1023	2.4958	1.8365	5.3349	5.6113
	LDS	0.8946	0.9381	0.8918	3.4484	1.2111	1.3066	1.6656	3.4262	2.3850	1.6333	2.7971	6.5685
2%	CMCN-PSO	1.1589	1.2517	1.0908	4.8594	2.0832	1.9856	2.0051	7.9203	3.2935	2.0461	5.3258	7.8713
	LHS	1.7186	1.9954	1.3693	5.5975	3.2203	3.4256	2.9096	10.6826	4.4206	4.7631	5.8981	16.1207
	LDS	1.4886	1.1975	1.2756	6.1999	2.1891	1.7512	2.4179	9.4052	3.4007	3.7081	4.1591	13.2061

TFI-HSS is transformed into an optimization problem of minimizing the loss function. Finally, the PINN model is trained to acquire the surrogate model of the reconstructed temperature field, where transfer learning strategy is used to accelerate the training process. However, noise observations significantly affect the reconstruction performance of the PINN-TFI method. To this end, the CMCN-PSO method is proposed to alleviate the effect of noise observations. We have proved the upper bound of the reconstruction error is related to the coefficient matrix condition number, which is determined by positions of noise observations. Subsequently, the condition number is used as the principle to find optima positions. After that, the PINN-TFI method with optima positions can achieve better reconstructed performance. Experiments have shown that the PINN-TFI method can reconstruct the temperature field well in the small data setting, where transfer learning strategy can accelerate training process significantly. Besides, the CMCN-PSO method can find optimal positions to alleviate the effect of noises under different noise levels and numbers of observations, making the PINN-TFI method to reconstruct a more robust temperature field. In future work, reducing the number of observations while maintaining reconstructed performances is an interesting research point.

Declaration of competing interest

The authors declare that they have no known competing financial interests or personal relationships that could have appeared to influence the work reported in this paper.

Replication of results

The code can be downloaded at: https://github.com/liuxu97531/PINN_TFI-HSS.

Acknowledgements

This work was supported by National Natural Science Foundation of China under Grant No.11725211, 52005505, and 62001502.

References

- M Grujicic, CL Zhao, and EC Dusel. The effect of thermal contact resistance on heat management in the electronic packaging. *Appl. Surf. Sci.*, 246(1-3):290–302, 2005.
- Eduardo Laloya, Oscar Lucia, Hector Sarnago, and Jose M Burdio. Heat management in power converters: From state of the art to future ultrahigh efficiency systems. *IEEE Trans. Power Electron.*, 31(11):7896–7908, 2015.
- Mohamed Emam, Shinichi Ookawara, and Mahmoud Ahmed. Thermal management of electronic devices and concentrator photovoltaic systems using phase change material heat sinks: Experimental investigations. *Renew. Energ.*, 141:322–339, 2019.
- Michael N Evans, Alexey Kaplan, and Mark A Cane. Pacific sea surface temperature field reconstruction from coral $\delta^{18}O$ data using reduced space objective analysis. *Paleoceanography*, 17(1):7–1, 2002.
- Qian Kong, Genshan Jiang, Yuechao Liu, and Miao Yu. Numerical and experimental study on temperature field reconstruction based on acoustic tomography. *Appl. Therm. Eng.*, 170:114720, 2020.
- Johan Frederik Steffensen. *Interpolation*. Courier Corporation, 2006.

- Michael L Stein. *Interpolation of spatial data: some theory for kriging*. Springer Science & Business Media, 2012.
- Mark R Segal. Machine learning benchmarks and random forest regression. 2004.
- Nan Jiang and Luo Wang. Quantum image scaling using nearest neighbor interpolation. *Quantum Inf Process*, 14(5): 1559–1571, 2015.
- C Le Niliot and F Lefèvre. A method for multiple steady line heat sources identification in a diffusive system: application to an experimental 2d problem. *Int. J. Heat Mass Transf.*, 44(7):1425–1438, 2001.
- C Le Niliot, Fabrice Rigollet, and D Petit. An experimental identification of line heat sources in a diffusive system using the boundary element method. *Int. J. Heat Mass Transf.*, 43(12):2205–2220, 2000.
- Ching-yu Yang. The determination of two heat sources in an inverse heat conduction problem. *Int. J. Heat Mass Transf.*, 42(2):345–356, 1999.
- Yong Shuai, Xiaochen Zhang, Hengxin Qing, and He-ping Tan. Inversion research on temperature field with nonlinear multiple heat source using i-deas, j. *Journal of Astronautics*, 32:2088–2095, 2011.
- Maziar Raissi, Paris Perdikaris, and George E Karniadakis. Physics-informed neural networks: A deep learning framework for solving forward and inverse problems involving nonlinear partial differential equations. *J. Comput. Phys.*, 378:686–707, 2019.
- Sheng Shen, Hao Lu, Mohammadkazem Sadoughi, Chao Hu, Venkat Nemani, Adam Thelen, Keith Webster, Matthew Darr, Jeff Sidon, and Shawn Kenny. A physics-informed deep learning approach for bearing fault detection. *Eng Appl Artif Intell*, 103:104295, 2021.
- Navid Zobeiry and Keith D Humfeld. A physics-informed machine learning approach for solving heat transfer equation in advanced manufacturing and engineering applications. *Eng Appl Artif Intell*, 101:104232, 2021.
- TN Narasimhan and PA Witherspoon. An integrated finite difference method for analyzing fluid flow in porous media. *Water Resour. Res.*, 12(1):57–64, 1976.
- Han Gao, Luning Sun, and Jian-Xun Wang. Phygeonet: Physics-informed geometry-adaptive convolutional neural networks for solving parametric pdes on irregular domain. *arXiv e-prints*, pages arXiv–2004, 2020.
- Philipp Grohs, Fabian Hornung, Arnulf Jentzen, and Philippe Von Wurstemberger. A proof that artificial neural networks overcome the curse of dimensionality in the numerical approximation of black-scholes partial differential equations. *arXiv preprint arXiv:1809.02362*, 2018.
- Alireza Yazdani, Lu Lu, Maziar Raissi, and George Em Karniadakis. Systems biology informed deep learning for inferring parameters and hidden dynamics. *PLoS Comput. Biol.*, 16(11):e1007575, 2020.
- Maziar Raissi, Alireza Yazdani, and George Em Karniadakis. Hidden fluid mechanics: Learning velocity and pressure fields from flow visualizations. *Science*, 367(6481):1026–1030, 2020.
- Alexandre M Tartakovsky, C Ortiz Marrero, Paris Perdikaris, Guzel D Tartakovsky, and David Barajas-Solano. Physics-informed deep neural networks for learning parameters and constitutive relationships in subsurface flow problems. *Water Resour. Res.*, 56(5):e2019WR026731, 2020.
- Francisco Sahli Costabal, Yibo Yang, Paris Perdikaris, Daniel E Hurtado, and Ellen Kuhl. Physics-informed neural networks for cardiac activation mapping. *Front. Phys.*, 8:42, 2020.
- Georgios Kissas, Yibo Yang, Eileen Hwuang, Walter R Witschey, John A Detre, and Paris Perdikaris. Machine learning in cardiovascular flows modeling: Predicting arterial blood pressure from non-invasive 4d flow mri data using physics-informed neural networks. *Comput Methods Appl Mech Eng*, 358:112623, 2020.
- Chao Song and Tariq Alkhalifah. Wavefield reconstruction inversion via machine learned functions. In *SEG Technical Program Expanded Abstracts 2020*, pages 1710–1714. Society of Exploration Geophysicists, 2020.
- Guofei Pang, Lu Lu, and George Em Karniadakis. fpinns: Fractional physics-informed neural networks. *SIAM J Sci Comput*, 41(4):A2603–A2626, 2019.
- Xiaoli Chen, Liu Yang, Jinqiao Duan, and George Em Karniadakis. Solving inverse stochastic problems from discrete particle observations using the fokker–planck equation and physics-informed neural networks. *SIAM J Sci Comput*, 43(3):B811–B830, 2021a.
- Liu Yang, Steve Hanneke, and Jaime Carbonell. A theory of transfer learning with applications to active learning. *Mach Learn*, 90(2):161–189, 2013.
- Yanki Aslan, Jan Puskely, and Alexander Yarovoy. Heat source layout optimization for two-dimensional heat conduction using iterative reweighted l1-norm convex minimization. *Int. J. Heat Mass Transf.*, 122:432–441, 2018.

- Kai Chen, Shuangfeng Wang, and Mengxuan Song. Optimization of heat source distribution for two-dimensional heat conduction using bionic method. *Int. J. Heat Mass Transf.*, 93:108–117, 2016.
- Xianqi Chen, Xiaoyu Zhao, Zhiqiang Gong, Jun Zhang, Weien Zhou, Xiaoqian Chen, and Wen Yao. A deep neural network surrogate modeling benchmark for temperature field prediction of heat source layout. *arXiv preprint arXiv:2103.11177*, 2021b.
- Robert Eymard, Thierry Gallouët, and Raphaële Herbin. Finite volume methods. *Handb. Stat.*, 7:713–1018, 2000.
- Martin Alnæs, Jan Blechta, Johan Hake, August Johansson, Benjamin Kehlet, Anders Logg, Chris Richardson, Johannes Ring, Marie E Rognes, and Garth N Wells. The fenics project version 1.5. *Archive of Numerical Software*, 3(100), 2015.
- Cristiano Cervellera, Mauro Gaggero, and Danilo Macciò. Low-discrepancy sampling for approximate dynamic programming with local approximators. *Comput Oper Res*, 43:108–115, 2014.
- Diederik P Kingma and Jimmy Ba. Adam: A method for stochastic optimization. *arXiv preprint arXiv:1412.6980*, 2014.
- Eric Schulz, Maarten Speekenbrink, and Andreas Krause. A tutorial on gaussian process regression: Modelling, exploring, and exploiting functions. *J Math Psychol*, 85:1–16, 2018.
- Fabian Pedregosa, Gaël Varoquaux, Alexandre Gramfort, Vincent Michel, Bertrand Thirion, Olivier Grisel, Mathieu Blondel, Peter Prettenhofer, Ron Weiss, Vincent Dubourg, et al. Scikit-learn: Machine learning in python. *J Mach Learn Res*, 12:2825–2830, 2011.